Composites Part B 265 (2023) 110961

Contents lists available at ScienceDirect

Composites Part B

journal homepage: www.elsevier.com/locate/compositesb

Effect of biocomposite mediated magnesium ionic micro-homeostasis on cell fate regulation and bone tissue regeneration

Jie Shen [a,b,c], Lei Yong [a], Bo Chen [d], Wei Qiao [e], Xinyun Zhai [f], Shuhan Wang [g], Yongcan Huang [a], Paul K. Chu [h], Binsheng Yu [a,*], KelvinW.K. Yeung [b,c,i,**]

[a] Shenzhen Key Laboratory of Spine Surgery, Department of Spine Surgery, Peking University Shenzhen Hospital, Shenzhen, 518000, China
[b] Department of Orthopaedics and Traumatology, The University of Hong Kong, Hong Kong S.A.R., 999077, China
[c] Shenzhen Key Laboratory for Innovative Technology in Orthopaedic Trauma, The University of Hong Kong Shenzhen Hospital, Shenzhen, 518000, China
[d] Department of Orthopaedics, Shanghai Key Laboratory for Prevention and Treatment of Bone and Joint Diseases, Shanghai Institute of Traumatology and Orthopaedics, Ruijin Hospital, Shanghai Jiao Tong University School of Medicine, Shanghai, 200025, China
[e] Applied Oral Sciences and Community Dental Care, Faculty of Dentistry, The University of Hong Kong, Hong Kong S.A.R., 999077, China
[f] School of Materials Science and Engineering, Nankai University, Tianjin, 300071, China
[g] Shenzhen Institute for Drug Control, Shenzhen Testing Center of Medical Devices, Shenzhen, 518057, China
[h] Department of Physics, Department of Materials Science & Engineering, and Department of Biomedical Engineering, City University of Hong Kong, Hong Kong S.A.R., 999077, China
[i] China Orthopaedic Regenerative Medicine Group (CORMed), Hangzhou, 310000, China

ARTICLE INFO

Handling Editor: Dr Hao Wang

Keywords:
Biocomposite
Aggregation structure
Ionic microenvironment
Cellular behavior
Immune modulation
Bone formation

ABSTRACT

Bioinorganic cations, that actively involved in many vital cellular activities, have been highlighted in regeneration and repair of tissues recently. However, researchers are still exploring how the sophisticated regulation of these bioactive factors within the microenvironment contribute to the process. Here, we established magnesium oxide homogeneously- and heterogeneously-embedded biocomposites to investigate the biological impacts that result from the different aggregation structure of the bioinorganic element. On the heterogeneous biocomposite, unbalanced microenvironment with erratic ion niche was provided, while stable ionic microenvironment was shown on the homogeneous biocomposite. Compared with the ionic micro-homeostasis, the heterogeneous micron-cluster-created unbalanced niche compromised cellular adhesion and proliferation by restraining the membrane extensions and downregulating the expression of proliferative genes. This unbalanced niche also motivated nonactivated macrophage polarized towards pro-inflammatory phenotype and induced high ratio of necrotic cell death by increasing the intracellular oxidative stress and decreasing the ATP content. After implantation, the homogeneous scaffold promoted tissue healing, whereas the immune responses were deteriorated and prolonged by heterogeneous scaffold, which leading to impaired bone regeneration. This study demonstrated the importance of biocomposite-established magnesium ionic micro-homeostasis on bone tissue regeneration and may inspires the future development of biomaterials.

1. Introduction

Tissue regenerations that occur at multiscale are extraordinarily sophisticated and dynamic processes which highly correlated to the temporal and spatial factors within local tissue microenvironments [1–3]. As being well demonstrated by the advanced researches in the fields of biology and engineering, cells are hypersensitive to the microenvironment surrounded [4,5]. The precisely control over the cellular local microenvironment is therefore an essential requirement for regenerative medicine and tissue engineering.

Based on the current understanding of tissue morphogenesis and cell-environment interactions, biomaterials have been developed greatly to establish delicate microenvironments that involve multiple signaling factors in order to assist and regulate cells to repair tissues [5–7]. Indeed, biomaterial is now a key element of the regenerative medicine and has evolved from mere mechanical supports, physical connections

* Corresponding author.
** Corresponding author. Department of Orthopaedics and Traumatology, The University of Hong Kong, Hong Kong S.A.R., 999077, China.
E-mail addresses: hpyubinsheng@hotmail.com (B. Yu), wkkyeung@hku.hk (KelvinW.K. Yeung).

https://doi.org/10.1016/j.compositesb.2023.110961
Received 31 May 2023; Received in revised form 1 July 2023; Accepted 21 August 2023
Available online 22 August 2023

or delivery vectors without deep insight of biological functions towards instructive mediums that modulate cellular behaviors *in vitro* and *in vivo* [8–10]. However, because of the complexity of the regenerative process, efficient biomaterials usually need to be customized with precise delivery of diverse factors to create ideal microenvironments for the regeneration of tissues [11,12]. In this regard, a better understanding of the cell-material microenvironment interactions is hence important for the designing of biomaterials that enable superior control over the cell fate and subsequent tissue functionalization.

Composite materials, that consist of a large variety of organic and/or inorganic components, are widely applied in biomedical applications [13–15]. For these materials, the importance of particle aggregation structure was widely recognized in regard of their stability, mechanical, electrical and optical properties, whereas, the influence of the aggregation structure on the biological performances was seldom mentioned [16–19]. To date, most of the studies have focused on the performances of biological cues under well-prepared conditions. However, complex situations may arise in scale productions and practical applications, during which, clusters resulting from aggregation of the effective factors were not uncommonly seen, but less effort was made to investigate their microenvironmental and biological impacts [20–22]. Regenerative processes are modulated not only by the temporal presentation of bioactive factors but also by spatial gradients of morphogens that regulate chemotactic cellular behaviors [23]. Both the temporal release and spatial position of bioactive factor from the biomaterials determined their therapeutic potential. Our previous research showed that only several micrometers away from the area with an appropriate Mg^{2+} concentration, a Mg^{2+} ion-deficient or excess micro00environment could be accompanied by altered cellular behaviors [24]. Although the spatiotemporal coordination of diverse intracellular biomolecules makes the cell adaptable to the extracellular environment. The biocomposites mediated drastic fluctuation of the microenvironmental homeostasis may still have great impact on the bioactivities of the cells.

The translational application of biomaterial is a time-consuming, expensive, and challenging process. Numerous products fail as they have not shown the expected benefit or even associated with marked adverse effects due to the spatiotemporal imbalance of bioactive factors [25–27]. In this study, to investigate how the aggregation structure of the bioactive factor affects microenvironment establishment, cell fate regulation, and bone tissue regeneration, bioinorganic element magnesium (Mg), which is essential in numerous cellular functions and tissue regenerative processes is employed. Following the fabrication of magnesium oxide (MgO) homogeneously- and heterogeneously-embedded biocomposites, *in vitro* and *in vivo* studies were performed to investigate the detailed cellular behaviors, inflammatory responses, bone tissue regenerative process and their underlying mechanism within the biocomposite-mediated microenvironments.

2. Materials and methods

2.1. Material preparation and characterizations

2.1.1. Preparation of surface modified nano magnesium oxide

In this study commercial nano-magnesium oxide (MgO) spheres with the particle size of 50 nm (Aladdin Reagent Inc., China) were used. To adjust the dispersion of the nano-MgO in the polymer matrices, a silane coupling agent 3-(Trimethoxysilyl)propyl methacrylate (TMSPM) (Sigma, USA) was adopted to treat the surface of the nano-MgO. Similar to our previous study [28], the general process of nano-MgO surface modification was as follow: 10 g of MgO nanoparticles were first added to 3 mL of TMSPM together with 2 mL of propylamine and 100 mL of cyclohexane. The working temperature was kept at 80 °C during mixing, and the mixture was continuously stirred for 3 h. Then silane-coated MgO nanoparticles were obtained after filtration and vacuum drying overnight. After the surface modification, two groups of MgO, TMSPM-coated nano-MgO (T-MgO) and untreated nano-MgO (U–MgO) were classified.

2.1.2. Preparation of MgO nanoparticles embedded biocomposites

Two kinds of Polycaprolactone/magnesium oxide biocomposites were fabricated by incorporating 6 g of untreated or surface modified magnesium oxide nanoparticles into 10 g of biodegradable macromolecule polycaprolactone (PCL, Sigma, USA, number-average molecular weight 80,000 g/mol) through a solution blending process in a mixer at 60 °C.

2.1.3. Morphological characterizations of the MgO clusters

MgO aggregate size distribution in suspension liquid was observed via transmission electron microscope (TEM, CM100, Philips) and measured by photon-correlation spectroscopy (PCS, Zetasizer Nano S, Malvern Instrument).

2.1.4. Surface and interface observation of the biocomposites

The surfaces and cross sections morphologies of the untreated MgO/PCL heterogeneous biocomposite (U–MgO/P) and TMSPM-coated MgO/PCL homogeneous biocomposite (T-MgO/P) before or after immersion for 7, 15 and 30 days were observed by scanning electron microscopy (SEM, S-4800 FEG, Hitachi). The magnesium and carbon elements distribution of each sample were measured together via energy-dispersive x-ray spectroscopy (EDS).

2.1.5. 3D-Reconstructed particle distribution within the biocomposites

The dispersion states of the particles within the biocomposites were reconstructed to 3D models based on the SEM micrographs using the method described in previous study [29]. In brief, the cross-section images of the materials were first digitized and formatted using an ImageJ software. Once the particles had been marked, the image dimensions, midpoint-coordinates and the areas of the particles were then exported to MATLAB to evaluate the radius and the center-to-center distance of the highlighted particles. Finally, the 3D models were reconstructed based on the size distribution of the MgO-particles as determined for all the biocomposites. Coefficient of variation (CV), the ratio of the standard deviation to the mean that shows the extent of variability in relation to the mean of the population, were calculated based on the cluster size of the two biocomposites.

2.1.6. Evaluation of particle distribution within the biocomposites by micro-computed tomography

To monitor the particle distribution in U–MgO/P and T-MgO/P, micro-computed tomography (μ-CT, SkyScan 1172, Bruker) was used to scan the biocomposites. The pixel size was fixed at 0.6 μm, the rotation step at 0.6° and exposure was performed with a 0.5-mm aluminum filter. The 2D planes were first reconstructed by the NRecon (Skyscan Company). Then, the 3D models of the composites were generated using CTVox (Skyscan Company). The CTAn program (Skyscan Company) was used to examine the particle-size distribution by morphometry and densitometry.

2.1.7. Ion-releasing profile measurement

Immersion tests were performed to working out the daily release profiles of magnesium ion (Mg^{2+}) from U–MgO/P and T-MgO-P biocomposites. The measurement procedure was as follow: three disc samples (diameter = 1 cm, weight = 0.05 g) of each composite were individually immersed into sealable capsules which containing 10 mL of simulated body fluid (SBF). The capsules were then incubated at 37 °C and the immersion fluids were daily refreshed for 15 days. The Mg^{2+} concentration of each sample was measured via inductively coupled plasma optical emission spectrometry (ICP-OES, Optima 2100DV, Perkin Elmer). After determining the Mg^{2+} concentration in daily changed SBF, the daily change rate of Mg^{2+} release from different composites were calculated by using the following equation S(1):

$$\% \Delta X = \frac{(B - A)}{A} \times 100\% \quad \text{(S1)}$$

where the A and B are the Mg^{2+} concentration of day y and day (y+1), respectively.

2.1.8. Monitoring of local spatial distribution of magnesium ions on the biocomposites

Scanning ion-selective electrode technique (SIET, BIO-001A, Younger USA Sci. and Tech. Corp.) as described in previously research [30] with small modification in Xu-Yue company (Beijing, China) was used to measure the net fluxes of Mg^{2+} over the surface of U–MgO/P and T-MgO/P. A selective microelectrode of the Mg^{2+} was used to map the net fluxes of Mg^{2+} sequentially 50 μm above the composite surfaces on a 5 × 5 grid after immersed in the measuring solution (8.059702 mM $Na_2HPO_4{\cdot}7H_2O$, 1.4705882 mM KH_2PO_4, 137.93103 mM NaCl, 2.6666667 mM KCl, 1 mM $MgCl_2{\cdot}7H_2O$) for 30 min. The obtained data then were analyzed and converted to specific ion outflow ($pmol{\cdot}cm^{-2}{\cdot}s^{-1}$).

2.2. Investigation of in vitro cellular behaviors on the composites

2.2.1. Observation of cell morphology on the biocomposites

Enhanced green fluorescent protein osteoblasts (eGFPOB) and MC3T3-E1 pre-osteoblast cells derived from mice were used in this study. High-glucose Dulbecco's Modified Eagle's Medium (DMEM) (Invitrogen, USA) was used to culture the cells. It was supplemented with 2 mM L-glutamine, 10% fetal bovine serum (FBS, Gibco, Australia), 100 mg/L streptomycin, and 100 U/ml penicillin. The incubation temperature was 37 °C with an atmosphere of 95% air and 5% CO_2.

To examine the cell morphologies shown on the biocomposites, eGFPOB with a cell density of 3×10^4 cells/cm^2 were first seeded onto the material surfaces in 96-well plates. Cells were cultured as described above. After culturing for 12 h, the adhesion morphology of the eGFPOB was observed via fluorescence microscopy (ECL IPSE 80i, Nikon). Quantitative analysis of cell membrane extensions was performed on isolated cells from ten randomly chosen fluorescence photomicrographs for each group. Three types of extensions, i.e., filopodia, lobopodia and lamellipodia were classified and averaged.

Cell morphologies along with the material surface morphologies were observed by using SEM (S–3400 N variable pressure SEM, Hitachi). Biocomposite specimens were firstly placed into 96-well plate, and the MC3T3-E1 pre-osteoblast or macrophage cell RAW264.7 was seeded with the cell density of 3×10^4 cells/cm^2. After incubation for 3 days the cells were washed by phosphate buffer saline (PBS) and fixed by 10% neutral buffered formalin for 1 h, followed by a brief wash again with PBS. Specimens were then dehydrated in an up-grading series of ethanol and thrice in absolute ethanol before they were carried out with air dry. Next, they were mounted on an aluminum stage and coated with platinum in a sputter coater (Bal-tec SCD 005 Sputter Coater) before viewed.

2.2.2. Cell proliferation property examined by gene expression

By measuring the relative messenger RNA (mRNA) expression levels of the cell proliferation markers including cyclin B1 (CCNB1), thymidine kinase 1 (TK1), BUB3 mitotic checkpoint protein (BUB3), proliferating cell nuclear antigen (PCNA) (the used primer pairs are shown in the Supplementary Table 1), the cell proliferation properties on the U–MgO/P and T-MgO/P composites were assessed using quantitative real-time polymerase chain reaction (RT-PCR) technique. Similar to the cell morphology observation, 3×10^4 cells/cm^2 MC3T3-E1 pre-osteoblast cells were incubated on the materials for 1 day or 3 days in 6-well tissue plates. At each time point, a TRIZOL (Invitrogen, USA) reagent was first used to isolate the total RNA of the cells cultured on different materials. The RNA was then separated into aqueous phase by adding the chloroform. The colorless upper aqueous phase was next transferred into a 1.5 mL tube with the adding of isopropanol to precipitate the RNA subsequently. The obtained RNA pellet of each group was washed with 75% ethanol three times and was dissolved into the RNase inhibitor (diethyl pyrocarbonate, DEPC) treated water in the end. A Nanodrop 1000 spectrophotometer (Thermo Scientific, USA) was used to assess the concentrations of the RNA. By following the manufacturer's instruction, 500 ng of total RNA was reverse-transcribed to complementary DNA (cDNA) using Superscript III (Invitrogen, USA). SYBR Green PCR Master Mix (Applied Biosystems, USA) was used to perform the real-time PCR with the using of the ABI prism 7900HT sequence detection system (Applied Biosystems, USA). Finally, the relative mRNA expression level of each gene was normalized to the glyceraldehyde-3-phosphate dehydrogenase (GAPDH) housekeeping gene by using Ct values.

2.2.3. Cell proliferation and death analyzed by flow cytometry

To investigate the cell proliferation and cell death exhibited on the different biocomposites, pre-osteoblast cells with a cell density of 3×10^4 cells/cm^2 were seeded onto the material surfaces in 6-well plates. After culturing for 1 day and 3 days, the pre-osteoblast cells were incubated with 1 μg/mL of Hoechst 33342 (Ho) solution (Thermo Scientific, USA) and 5 μg/mL of propidium iodide (PI, Thermo Scientific, USA) in the DMEM culture medium for 30 min at 37 °C. Then the cells were collected and cooled to 4 °C, centrifuged at 300 g for 5 min, resuspended in PBS for test. Flow cytometry analysis was then performed on an FACSAria™ SORP cytometer (BD Biosciences, USA) with a flow rate of 300 cells·s^{-1}. The data were analyzed by FlowJo 10.4 software (Tree Star, USA).

2.2.4. Microscopic examination of cell death

Double fluorescent staining was further used to observe the dead cell on the U–MgO/P and T-MgO/P. Similar to the procedure for the flow cytometry analysis, after culturing for 1 day and 3 days, the MC3T3-E1 cell and macrophage cell RAW264.7 were incubated with 1 μg/mL of Ho solution and 5 μg/mL of PI in the DMEM culture medium for 30 min at 37 °C. And the cells were then observed via fluorescence microscopy (Nikon ECL IPSE 80i). The quantitative analysis of the cell death rate was counted from 5 random fluorescent photomicrographs.

2.2.5. Measurement of lactate dehydrogenase in supernatant

The cell viability of the cells was assessed by the lactate dehydrogenase (LDH) assay (Sigma-Aldrich, USA), which is a means of measuring membrane integrity as a function of the amount of cytoplasmic LDH released into the medium. The assay was performed according to the instruction provided by the supplier. In brief, after culturing on the U–MgO/P and T-MgO/P for 1 and 3 days, cells in 96-well plate were centrifuged at 250 g for 5 min. The supernatant was then transferred to a new flat-bottom plate. Equal volumes of LDH assay dye, LDH assay substrate and cofactor were mixed and added to each well in a volume equal to twice the volume of medium removed for testing. After incubated for 30 min at room temperature it was stopped by 0.1 M hydrochloric acid (HCl). Finally, optical density (OD) values were recorded by a microplate photometer (Thermo Scientific, USA) at 490 nm wavelength.

2.2.6. Measurement of caspase-3 activity

The caspase-3 like protease activity in the lysate was measured by using a caspase 3 colorimetric assay kit (Sigma-Aldrich, USA) according to the instruction provided by the supplier. Briefly, after cultured on the U–MgO/P and T-MgO/P for 1 and 3 days, pre-osteoblast cells were pelleted, washed and lysed to obtain cell lysates. Then a total volume of 100 μL reaction mixture which containing 10 μL of the caspase 3 Ac-DEVD-pNA substrate and 5 μL of cell lysate in assay buffer was measured at 405 nm wavelength by a microplate photometer (Thermo Scientific, USA) after 90 min incubation at 37 °C. At the same time, a control reaction mixture consists of 10 μL of caspase 3 inhibitor Ac-DEVD-CHO, 10 μL of the caspase 3 substrate and 5 μL of cell lysate in assay buffer was also employ to account for the non-specific hydrolysis

of the substrate.

2.2.7. Measurements of intracellular oxidative stress

The reactive oxygen species (ROS) level of pre-osteoblast cells cultured on U–MgO/P and T-MgO/P were measured with a fluorescent probe 2′,7′-dichlorofluorescin diacetate (DCFH-DA, Sigma, USA). After the pre-osteoblast cells were cultured on the materials for 1 and 3 days, they were carefully washed with PBS and stained at 37 °C for 20 min by DCFH-DA solution which contain 20 μM of DCFH-DA in the FBS-free DMEM. Afterward, the cells were washed again and followed by the measurement of the ROS level. The light emission was collected at 535 nm after the fluorochrome was excited at 488 nm by using a microplate reader (DTX 880, Beckman Coulter, USA).

2.2.8. Determination of ATP Content

The intercellular ATP content was quantitated by using a luciferin-luciferase reaction according to the supplier's instruction. The pre-osteoblast cells with a density of 3×10^4 cells/cm^2 were cultured on different composites for 1 and 3 days. At each time point, ATP was extracted by suspending the cells in extraction buffer (4 mM EDTA, 50 mM $MgCl_2$ and 20 mM glycine, pH 7.4) and heating in boiling water bath for 45 s. Then, 20 μL of the sample prepared was added into 100 μL firefly lantern extract solution (Sigma, USA) in a black 96-well plate. The intensity of the emission was examined 20 s later with a microplate reader (DTX 880, Beckman Coulter, USA).

2.2.9. Macrophage polarization analyses

The flow cytometry was also used to evaluate the polarization of macrophages cultured on the U–MgO/P and T-MgO/P. The representative markers of the pro-inflammatory and anti-inflammatory macrophage phenotypes employed in this study were the CD197 and CD206, respectively. In brief, after three days of culturing, the cells were collected and blocked with 1% bull serum albumin (BSA) for 30 min. Then, they were stained by Alexa Fluor 647-conjugated anti-mouse CD197 antibody (BD Pharmingen, USA, 1:100) and Alexa Fluor 488-conjugated anti-mouse CD206 antibody (BioLegend, USA, 1:100) at 4 °C for 30 min. The macrophages stained with rat IgG2a, κ Alexa Fluor® 488 (BioLegend, USA, 1:100) and rat IgG2a, κ Alexa Fluor® 647 (BD Pharmingen, USA, 1:100) were employed as the isotype controls. Finally, cell suspensions were analyzed on a BD FACSCantoII Analyzer (BD Biosciences, USA) with a flow rate of 300 cells·s^{-1}. The data were also analyzed by the FlowJo 10.4 software and cells directly cultured on the 6-well plate was used as control.

The RT-PCR technique was also employed to determine the expression levels of the pro-inflammatory macrophage phenotype related genes interleukin 6 (IL6), C–C chemokine receptor type 7 (CCR7 or CD197), cluster of differentiation 80 (CD80), tumor necrosis factor (TNF) and anti-inflammatory macrophage phenotype related genes interleukin 4 (IL4), interleukin 10 (IL10), mannose receptor C-type 1 (MRC1 or CD206), transforming growth factor beta 1 (TGFB1) (the used primer pairs are shown in the Supplementary Table 1). Similar to the method mentioned above, RAW264.7 cells were cultured on the U–MgO/P and T-MgO/P for 3 days in 6-well tissue plates with a cell density of 3×10^4 cells/cm^2, then the total RNA of the cells was harvested using the TRIZOL reagent. After the purification and reverse transcription steps, the quantitative gene analysis was conducted by the real-time PCR with the using of the ABI prism 7900HT sequence detection system. Finally, the relative mRNA expression level of each gene was normalized to the GAPDH housekeeping gene by using Ct values.

2.3. In vivo studies

2.3.1. The preparation of 3D printed scaffolds and surgical procedures of the animal study

The preparation procedure of the 3D scaffolds was based on a low-temperature extrusion-based additive manufacturing technique. In brief, 30% (weight percent) of the composites were dissolved in 1,4-Dioxane (Sigma, USA) solvent to form gel-like solutions. Then, the 3D scaffolds were manufactured via the extrusion-based rapid-prototyping machine (gesim biosacffolder2.1, Germany) on a −30 °C cooling stage. After printing, all of the scaffolds were lyophilized for 72 h before use.

The examined protocols of anesthetic, surgical and post-operative care of the animal study were all fulfilled the requests stated by the Licensing Office of the Department of Health of the Hong Kong Government and the University Ethics Committee of The University of Hong Kong (HKU).

For the subcutaneous implantation model, sixteen female BALB/c mice with the age of 8 week offered by the laboratory animal unit (LAU) of the HKU were used in this study. The average weights of the rats were approximately 25 g. During the surgery, the mice were anaesthetized with a combination of xylazine (6 mg/kg) and ketamine (67 mg/kg), shaved and followed by subcutaneous incision. Two different samples, U–MgO/P and T-MgO/P scaffolds, were subcutaneously implanted into two separate incisions on the back of each mouse, near the nape of the neck. Finally, the wound was sutured layer by layer. And all the mice were carefully monitored during the following three days by animal care services. Three-, seven-, fourteen-days, and twenty-eight-days post-implantation, the mice were euthanized by over dosage of Pentobarbital. The dorsal section containing composite scaffolds were carefully resected and fixed in 10% formalin for 48 h. The samples were then kept in 70% ethanol before the paraffin embedding.

For the hard tissue repairing model, twelve 12-week-old female Sprague-Dawley (SD) rats offered by the LAU were used in this study. Their average weight was approximately 300 g. During the surgery, the mice were anaesthetized with a combination of xylazine (6 mg/kg) and ketamine (67 mg/kg). The operational site was chosen on the lateral epicondyle. Rats were implanted with printed 3D scaffold samples on bilateral lateral epicondyle. To monitor the *in-vivo* immune responses and bone formation within the U–MgO/P and T-MgO/P implants, serial time points, i.e., 3, 7, and 28 days were set. During the surgery, the rats were anaesthetized, shaved and followed by decortication. A minimally invasive approach was then adopted to make a 2-mm diameter hole through the lateral epicondyle using a hand drill. Subsequently, a 3D scaffold sample was implanted into the holes prepared on the femur of the rat. Finally, the wound was sutured layer by layer with a proper dressing applied over the incision. At each time point, the rats were euthanized by over dosage of Pentobarbital. The femurs were collected and fixed in 10% formalin for 48 h followed by the decalcification or the hard tissue processing procedure.

2.3.2. Histological and immunohistofluorescence analyses

After 3-, 7-, 14- and 28-days implantation, subcutaneous tissue samples were fixed, paraffin-embedded and sectioned at a 5 μm thickness. All the samples were then undergone Hematoxylin and Eosin (H&E) staining while the 28-day samples were stained by Masson' s trichrome staining per manufacturer's protocol. Three-, seven- and twenty-eight-days post-operation, the femoral samples were also fixed, decalcified, paraffin-embedded and sectioned at a 5 μm thickness. The sectioned specimens were stained via H&E, Masson' s trichrome or Safranin O/Fast Green staining, and a light microscope was used to perform the histological analyses. Immunofluorescence staining was conducted to further assess the immune response or bone formation of the tissues with the use of CD 68 (Abcam, UK), iNOS (Abcam, UK), CD 163 (Abcam, UK) or OCN (Abcam, UK) anti-bodies.

Four-weeks post-operation, the femurs of the euthanized rats also underwent hard tissue processing. For the hard tissue processing, similar to the previous study [28], standard steps were conducted after the tissues were fixed for 48 h. Briefly, dehydration of the tissues in a gradient concentration of ethanol was employed first (70% × 1, 95% × 1, 100% × 2, a three-day immersion for each change). Then, xylene was used for another three-day immersion before three stages of different

methyl methacrylate (i.e., MMA I, II, and III, changed every four days, MERCK, Germany). The specimens were finally put into a 37 °C environment to polymerize the MMA after being immersed in the MMA III. The embedded tissues were then cut into sections and micro-grinding down to ~50 μm thickness for Giemsa staining.

2.3.3. The evaluation of new bone formation by micro-computed tomography

To assess the new bone formation within the defect site, the rats were scanned by a micro-computed tomography (μ-CT, SKYSCAN 1076, Skyscan Company) instrument at two and four weeks. The reconstruct of 2D planes and the analysis of new bone growth by densitometry and morphometry were also performed by the NRecon and CTAn programs, while 3D models of newly formed bone within the implants were reconstructed by employing a CTVol program (Skyscan Company).

2.3.4. Mechanical properties of newly formed bone

The Young's modulus and the surface hardness of the newly formed bone within the defect was evaluated by a nanoindentation test (Nano Indenter G200, USA). The depth limit and drift rate were set as 2000 nm and 0.5 nm s^{-1}, respectively. Each sample was indented five times and three samples in each group were measured for statistical significance.

2.4. Statistical analysis

The *in vitro* experiments were conducted in triplicate. The *in vitro* and *in vivo* experimental data were analyzed by a one-way analysis of variance and expressed as means standard deviations. A p value < 0.05 was

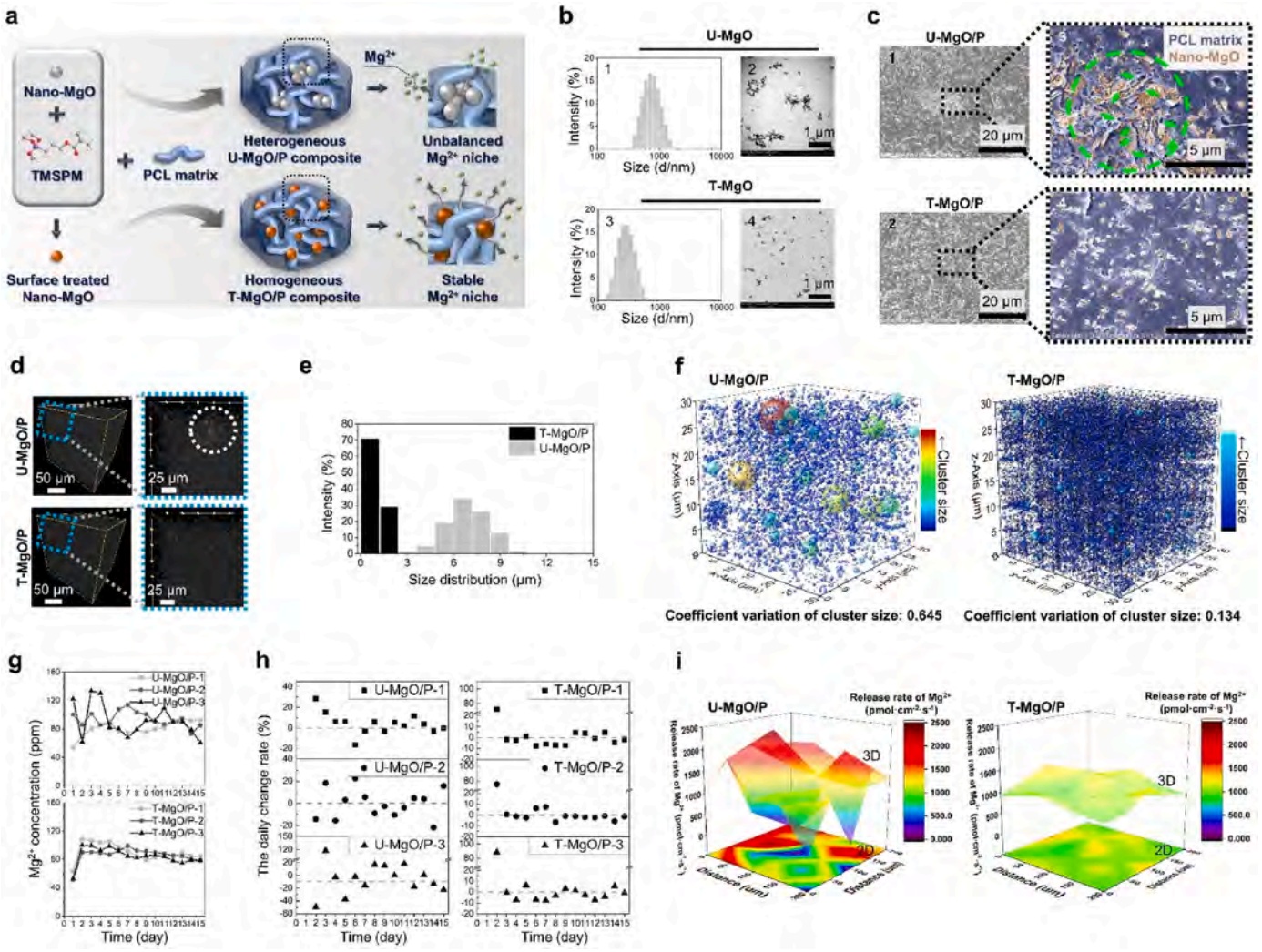

Fig. 1. Preparation and characterization of heterogeneous (U–MgO/P) and homogeneous (T-MgO/P) biocomposites. (a) Preparation process of U–MgO/P and T-MgO/P biocomposites. After the surface treatment of the MgO, biocomposites were fabricated via a solution blending process with the PCL and MgO. (b) 1) U–MgO and 3) T-MgO cluster size distribution along with 2) U–MgO and 4) T-MgO TEM observation in suspension liquid. Better distribution of the nanoparticles was found in T-MgO sample. Scale bar: 1 μm. (c) Cross Section morphologies of the 1) U–MgO/P and 2) T-MgO/P with 2000 times magnification and the 3) U–MgO/P and 4) T-MgO/P with 10000 times magnification. The micron-clustered site is figured out in the green dashed circle and some defects among the MgO nanoparticles and between the PCL and MgO phase are pointed out with green arrows. Scale bar: left 20 μm, right 5 μm. (d) Micro-CT 3D reconstruction models of the biocomposites and (e) statistics of particle size distributions within the 3D models. The big agglomeration site is figured out in the white dashed circle. (f) The reconstruction of the U–MgO/P and T-MgO/P biocomposites and coefficient of variation based on the size distribution of the MgO clusters. (g) Daily magnesium ion release of U–MgO/P and T-MgO/P biocomposites immersed in 10 mL simulated body fluid (SBF) (37 °C incubator, the immersion fluid was daily refreshed. Diameter of each disc sample = 1 cm, weight = 0.05 g). (h) Daily change rate of Mg^{2+} release from U–MgO/P and T-MgO/P biocomposites. % ΔX = (B–A)/A*100%; A = The Mg^{2+} concentration of day y; B = The Mg^{2+} concentration of day (y+1). (i) Magnesium ion release rate mapping over the scanned area of U–MgO/P and T-MgO/P surface. The specific magnesium ion outflow rate over the surface of U–MgO/P is extremely erratic while the T-MgO/P biocomposite exhibits evenly ion release. (For interpretation of the references to color in this figure legend, the reader is referred to the Web version of this article.)

considered to be statistically significant.

3. Results

3.1. Preparation and characterizations of the biocomposite materials

3.1.1. Preparation and morphological characterizations of MgO clusters

The fabrication procedures of the surface treated MgO and biocomposite materials are illustrated in Fig. 1a, while Fig. 1b shows the size distribution of different clustered samples in suspension liquid. The aggregate size distribution of both untreated U–MgO and surface-modified T-MgO obey the normal distribution. The diameter of the U–MgO microclusters ranging from 400 nm to 2 μm while the average diameter of the T-MgO nanoclusters was only 297 nm. As it can be clearly seen in Figs. 1b–2 and 1b-4, the T-MgO has an obviously homogeneous and nanoscale size distribution, in contrast, dozens to hundreds of the U–MgO nanoparticles aggregate together at microscale in the area observed.

3.1.2. Interface observation of the biocomposites

To observe the morphological differences between the heterogeneous biocomposite U–MgO/P and homogeneous biocomposite T-MgO/P, the cross sections morphologies of the biocomposites were observed and compared (Fig. 1c and Supplementary Fig. 1). Numerous microscale clusters distributed in the cross-sectional area of U–MgO/P. The aggregation site can be clearly seen within the green dashed circle (Figs. 1c–3), where not only aggregate of the MgO nanoparticles but also some level of phase separation due to the incompatibility between the polycaprolactone (PCL) matrix and inorganic phase can be observed. Without being embedded by the polymer matrix, the MgO could have a higher reaction rate with water compared to the PCL infiltrated MgO. To make it worse, the defect sites, which were pointed out with green arrows, might accelerate the process of uncontrolled release, because of the larger interface between MgO and water. However, as shown in Figs. 1c–4, aggregation of the nanoscale particles is efficaciously prevented within the T-MgO/P, obtaining homogeneously distributed MgO. Significantly improvement of the connection between the PCL and MgO can also be observed, which leading to a remarkable interface quality in the T-MgO/P.

3.1.3. Particle distribution within the biocomposites

The distribution of the MgO particles within the two biocomposites was studied using 3D reconstructed models (Fig. 1f), which based on multiple scanning electron microscope (SEM) micrographs. The smallest particles represent as the single nano-MgO, whereas larger particles represent the clusters of the MgO. The U–MgO nanoparticles were mainly present inside large clusters of the size ranging from *ca.* 1 μm–10 μm, with the polymer matrix intercalated. In sharp contrast, the T-MgO

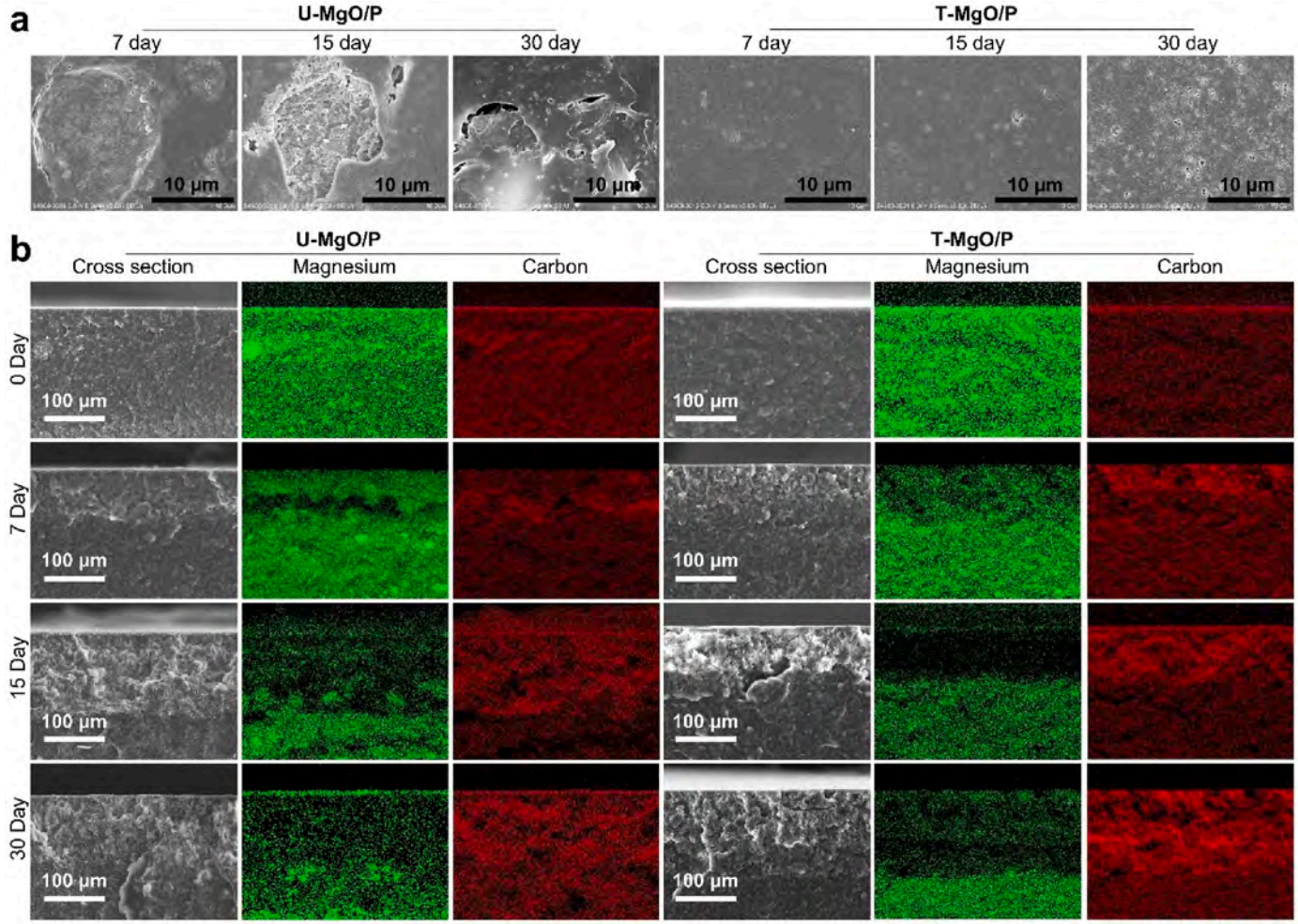

Fig. 2. Morphological observation of the U–MgO/P and T-MgO/P composites after immersion. (a) Surface morphologies of the U–MgO/P and T-MgO/P after SBF immersion for 7, 15 and 30 days. Irregular holes distributed randomly on the surface of the U–MgO/P with the pore size ranged from several to tens micrometers while pores homogeneously distributed on the T-MgO/P with the size from few tens nanometers to a micron in range. Scale bar: 10 μm. (b) Cross section morphologies along with the corresponding magnesium and carbon element distributions of the U–MgO/P and T-MgO/P hybrids before and after immersion in SBF for 7, 15 and 30 days. Scale bar: 100 μm.

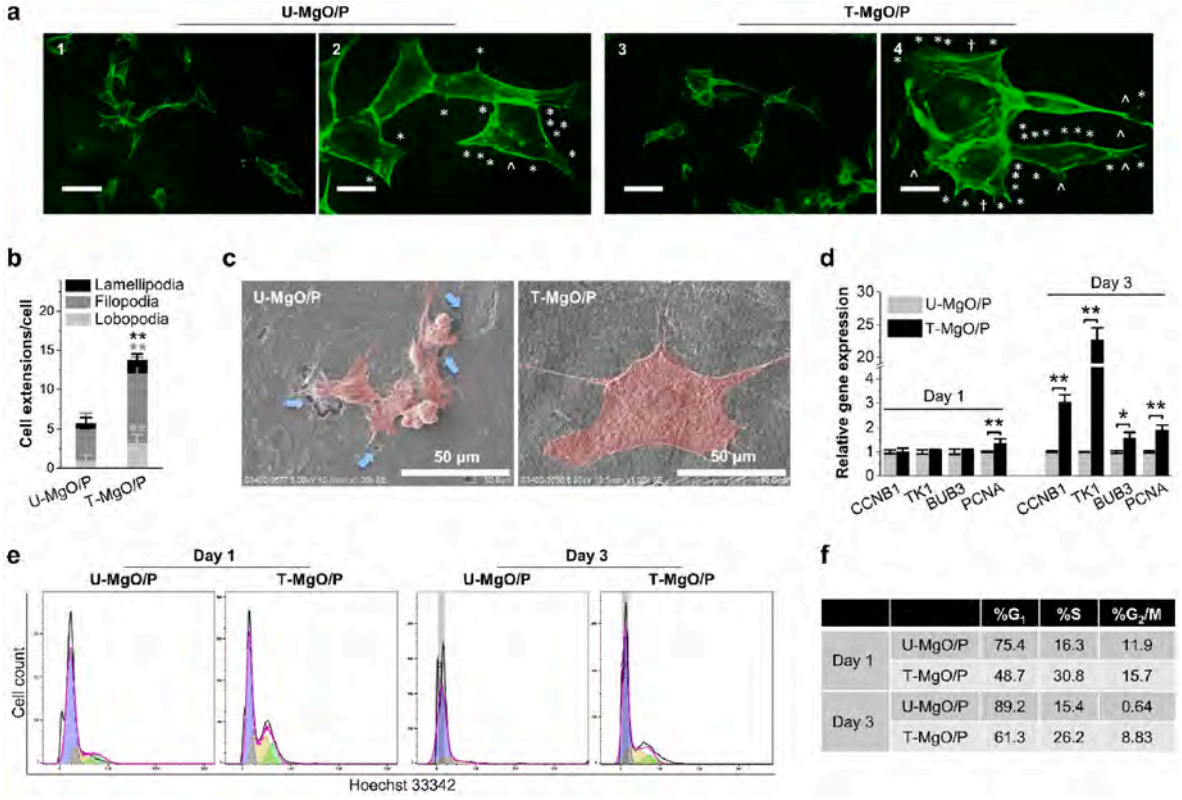

		%G_1	%S	%G_2/M
Day 1	U-MgO/P	75.4	16.3	11.9
	T-MgO/P	48.7	30.8	15.7
Day 3	U-MgO/P	89.2	15.4	0.64
	T-MgO/P	61.3	26.2	8.83

Fig. 3. Morphological observation and cell proliferation on the U–MgO/P and T-MgO/P biocomposites. (a) morphologic observation of fluorescent cell on U–MgO/P and T-MgO/P biocomposites. 200 times magnification microscopic views of cell cultured on 1) U–MgO/P and 3) T-MgO/P after 12 h to evaluate the cell adhesion and cytocompatibility of the materials. Scale bar: 100 μm. 2) U–MgO/P and 4) T-MgO/P with 800 times magnification. Lamellipodia, filopodia and lobopodian of the cells are indicated by †, * and ^, respectively. Scale bar: 25 μm. (b) Quantitative analysis of cell membrane extensions. The projections of the membrane per cell were analyzed from the fluorescent images. Average numbers of the lamellipodia, filopodia and lobopodian of each cell from T-MgO/P were all significantly higher than the extensions from the U–MgO/P group. (c) Cell morphologies after culturing for 3 days on U–MgO/P and T-MgO/P surfaces. Cells around pores (blue arrows) shrank while cells exhibit good spreading on the surface without obvious micropores. Scale bar: 50 μm. (d) Analysis of cellular proliferation properties via the mRNA expression level measurement. The mRNA expression levels of four proliferation markers were measured and normalized to the housekeeping gene. Compare to the U–MgO/P group, significantly higher expression levels of all the genes can be found in T-MgO/P group at day 3. (e) and (f) Cell cycle analysis on different biocomposites. Ho-stained cells were analyzed by flow cytometry and FlowJo Software. (e) DNA histograms with curve fitting of different cell-cycle phases were analyzed using FlowJo Software. (f) Quantitative analysis of the cell cycle population on the U–MgO/P and T-MgO/P. Compared to the T-MgO/P, the U–MgO/P induces cell cycle arrest. (*, $p < 0.05$; **, $p < 0.01$). (For interpretation of the references to color in this figure legend, the reader is referred to the Web version of this article.)

nanoparticles were distributed homogeneously over the entire model, with the nanoscale distribution pervaded. The coefficient variation of the cluster size within the U–MgO/P and T-MgO/P are 0.645 and 0.134, respectively. Generation of the biocomposite 3D models and statistics of the particle size distributions within the 3D models were further conducted after the micro-computed tomography (micro-CT) scanning (Fig. 1d and e). Similar to the SEM observation, even distribution of MgO was exhibited without any obvious aggregation inside the T-MgO/P, while micron-sized clusters can also be seen within the U–MgO/P biocomposite. The quantitative analysis showed a highly monodispersed size distribution of the T-MgO inside the T-MgO/P biocomposite, while polydisperse size distribution of the MgO micron-clusters was found within the U–MgO/P (3–11 μm).

3.1.4. Release profile and local spatial distribution of magnesium ions from the biocomposites

The daily release rates of magnesium ion (Mg^{2+}) from the U–MgO/P and T-MgO/P biocomposites were then working out by using immersion tests (Fig. 1g). The Mg^{2+} released from each sample of the T-MgO/P group are found from around 100 ppm/day at day 2 steadily decreased to around 80 ppm/day at day 15. The Mg^{2+} daily release rates of the U–MgO/P specimens, by contrast, were irregular and show large fluctuations, which are found in the range of 54–130 ppm/day. From the data shown in Fig. 1h, it can be figured out that compare to the U–MgO/P group, the T-MgO/P group has a more stable Mg^{2+} daily release. Except the 2nd day, the daily change rates of the T-MgO/P are in the range of ±8% from the 2nd day to the 15th day, whereas the change rates of the U–MgO/P group shows a wide scale from −50% to 118%. Moreover, obvious differences of the net fluxes of Mg^{2+} over the surface can be observed between the heterogeneous and homogeneous materials (Fig. 1i). The specific outflow rate over the surface of U–MgO/P is extremely erratic from several hundred pmol·cm^{-2}·s^{-1} to over 2000 pmol cm^{-2}·s^{-1}. In sharp contrast, the T-MgO/P biocomposite exhibits evenly ion release which is in a narrow range from 870 to 1380 pmol cm^{-2}·s^{-1}.

3.1.5. Surface and interface observation of the biocomposites after immersion

The surface morphological change of the U–MgO/P and T-MgO/P after immersion for 7, 15 and 30 days were observed by SEM (Fig. 2a). After 7 days immersion, huge sunken areas with the diameter up to a dozen of micron as well as tens-of-micrometers-long cracks appear on the surface of U–MgO/P. Interestingly, the inner sites of the U–MgO/P are exposed after the surface layer disappeared at day 15. As a result, large amount of MgO clusters appear within the low-lying areas, as well as deep holes without any MgO observed. The react between the MgO

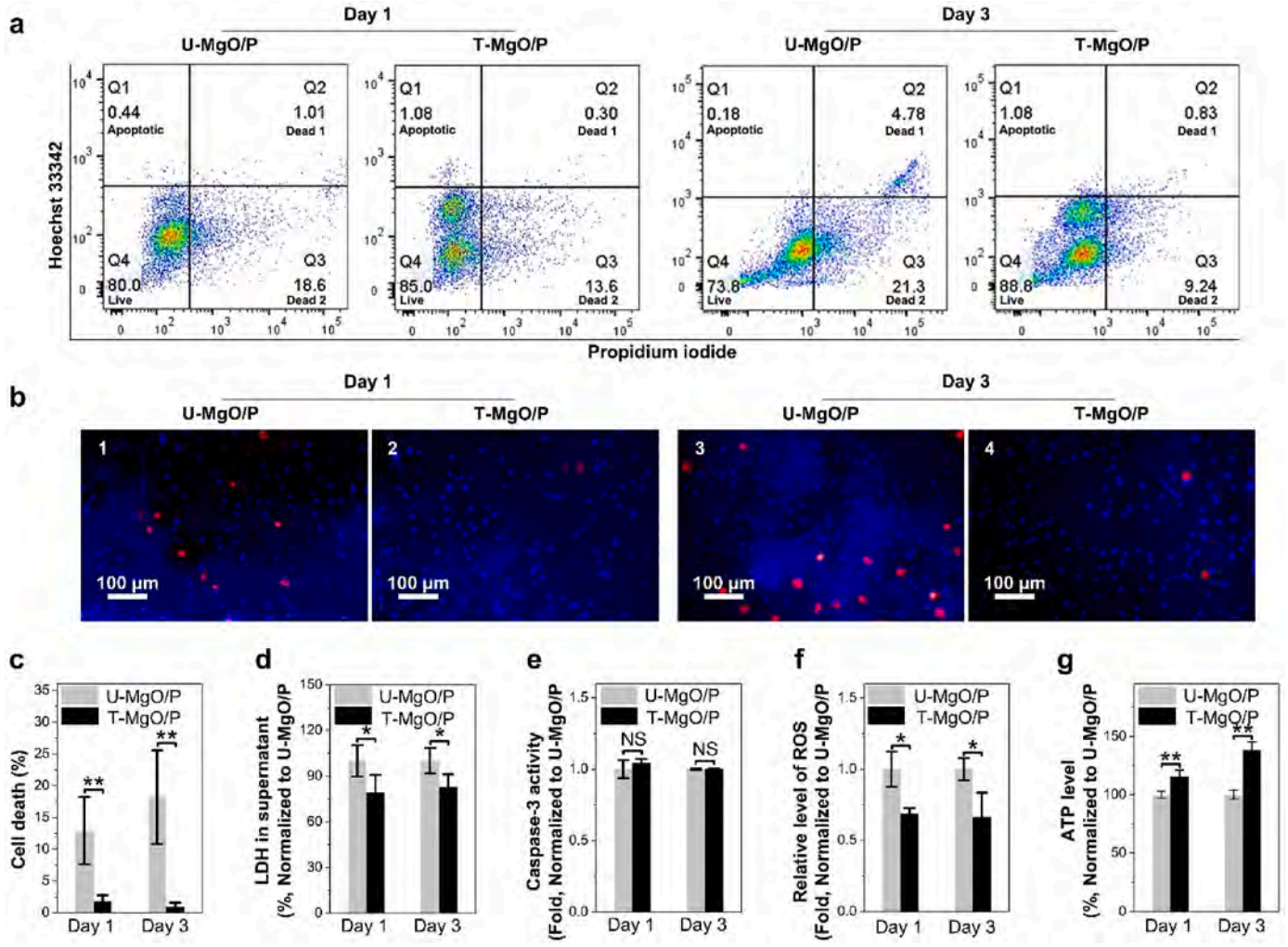

Fig. 4. Death of cells on the U–MgO/P and T-MgO/P biocomposites. (a) Death rate of the cells determined by the Ho and PI double staining using flow cytometry. The red fluorescence intensity from PI allows discrimination of dead cells. And double negative indicates the live cell population. (b) Fluorescence microscopic observation and (c) quantitative analysis of the cell death rate of the cells cultured on the U–MgO/P and T-MgO/P. (d) The membrane integrity of cells cultured on U–MgO/P and T-MgO/P assessed by the LDH assay. With the Mg^{2+} micro-homeostasis, the LDH leakage of the cells cultured on the homogeneous T-MgO/P was significantly lower than on the heterogeneous U–MgO/P. (e) The caspase-3 activities of cells cultured on different biocomposites. Almost the same values were obtained from the U–MgO/P and T-MgO/P groups. (f) The ROS levels of cells cultured on U–MgO/P and T-MgO/P. The cells cultured on the U–MgO/P showed increased ROS levels at all time points compared to the T-MgO/P group. (g) The intercellular ATP contents of cells cultured on U–MgO/P and T-MgO/P. The intracellular ATP level is a critical factor of the cell's decision to die through necrosis or apoptosis. The ATP content of the cells cultured on the U–MgO/T was significantly lower in comparison with the T-MgO/P group. (*, $p < 0.05$; **, $p < 0.01$; NS, no significant difference). (For interpretation of the references to color in this figure legend, the reader is referred to the Web version of this article.)

and water would mainly concentrate at the micron-cluster sites primarily. At this stage, burst or uneven release occur on the U–MgO/P. Finally, after 30 days of immersion, plenty of irregular empty holes distributed randomly on the surface of the U–MgO/P with the pore size ranged from several to tens micrometers. In contrast to the U–MgO/P specimen, only a few nano-scale pores appear on the surface of the T-MgO/P after 7 days immersion in SBF. The pores homogeneously distributed on the T-MgO/P after 30 days immersion are all with the size from few tens nanometers to a micron in range. Then, the cross sections morphologies along with the corresponding magnesium and carbon elements distributions of the biocomposites were observed (Fig. 2b). Before the immersion, micron-scaled magnesium agglomerates appear from U–MgO/P while the T-MgO/P has a visible homogeneous magnesium element distribution. After immersing for 7 days, dark areas which represent low Mg element abundance appear within the depth from 40 to 60 μm, and large MgO aggregates can still be found in the deeper site of U–MgO/P. The dark areas become larger in size and converged together reaching the depth of 200 μm after 15 days of immersion. In the end, large area observed from the U–MgO/P shows low Mg elementary intensity. However, with the homogeneous dispersion of T-MgO, T-MgO/P biocomposites reveal gradual and moderate decrease of Mg element intensity that from the outer surface to the inner part of the material.

3.2. Investigation of in vitro cellular behaviors on the biocomposites

3.2.1. Observation of cell morphology on the biocomposites

To examine the cell morphologies shown on the biocomposites, enhanced green fluorescent protein osteoblasts seeded on the materials were observed and cell membrane projections were quantified (Fig. 3a and b). The extensions, e.g., filopodia, lobopodian and lamellipodia are indicated in the figures with 400 times magnification by the symbols *, ˆ and †, respectively. A considerable amount of extended microspikes filopodia can be observed from the cells grown on the T-MgO/P. The number of the projections extended by the eGFPOB on T-MgO/P biocomposite is much greater than the U–MgO/P group. Average numbers

of the lamellipodia, filopodia and lobopodian of each cell from T-MgO/P were all significantly higher than the extensions from the U–MgO/P group. Cell morphologies presented on the two biocomposites were then observed using SEM (Fig. 3c). The U–MgO/P which forms tens of micron-sized randomly distributed irregular pores (blue arrows) on the surface yield in round and crimpled morphologies of the cells around the pores. Without any obvious micropores appear, cells which are totally spread display flattened morphology on the T-MgO/P surface. Compare to the cells adhere on the U–MgO/P surface, the cells show larger cell surface area and long filopodia on the T-MgO/P.

3.2.2. Examination of cell proliferation property on the biocomposites

To evaluate the proliferation properties of the cell cultured on different biocomposites, the expression level of specific target genes including CCNB1, BUB3, TK1 and PCNA were determined (Fig. 3d). After 24 h culturing, the CCNB1, TK1 and BUB3 genes stay at almost same level, while the PCNA gene, a well-known marker for cycling cell, shows a significantly increase of expression by the cell grown on the T-MgO/P. On day 3, all the genes are upregulated significantly (range between 1.6- and 22-fold) in T-MgO/P group as compared to U–MgO/P group. The TK1 gene, which is closely related to cell division, high in proliferating cells and peaks during the S-phase of the cell cycle, shows a dramatic 22-fold enhancement of expression as against the U–MgO/P. Cell cycle was analyzed by flow cytometry method using Hoechst 33342 cell permeable dye (Fig. 3e and f). Two obvious peaks, which attributed to the G_1 and G_2/M populations, can be observed from T-MgO/P group in both day one and day three figures. By contrast, there is almost no G_2/M peak shown in U–MgO/P group after three days of culturing, suggesting a blockade in cell cycle progression. The calculated percentage also confirmed that, in this group, 75.4% and 89.2% of the population was in the G_1 phase at day one and three, respectively. Cultured on the U–MgO/P, only around 15% of the population was in the S phase at these two time points, while T-MgO/P group has almost doubled S-phase population. Studies have demonstrated that both magnesium deficiency and excess could inhibit the growth of cells [31,32]. Cells would also not recover from extraordinarily high content of intracellular Mg^{2+} [32].

3.2.3. Examination of cell death on the biocomposites

To distinguish viable cells from death, cells were analyzed by flow cytometer with Hoechst 33342 blue fluorescence and propidium iodide red fluorescence as functions of Ho/PI (Fig. 4a). High red fluorescence intensity (abscissa axis) allows discrimination of dead cells, and double negative indicates the live cell population. After 1 and 3 days of culturing, 19.61% and 25.08% cell died on the U–MgO/P. Meanwhile, the values of T-MgO/P group are only 13.9% and 10.17%, respectively. These results can be also confirmed by the fluorescence microscopic observation (Fig. 4b). Tens of dead cells can be found on the U–MgO/P while barely one or two red-stained cells on T-MgO/P. Quantitative analysis of the cell death rate from fluorescent photomicrographs shows that, after 1 and 3 days of culturing, 12.93% and 18.18% cells died on the U–MgO/P, by contrast, the number from T-MgO/P group were all under 3% (Fig. 4c).

The cell membrane integrity and cell viability were then evaluated by the lactate dehydrogenase (LDH) assay (Fig. 4d), which exhibited the impact of the cluster-created Mg^{2+} microenvironment on membrane integrity. With the stable Mg^{2+} micro-homeostasis, the cells cultured on the T-MgO/P showed 20% lower LDH leakage than on the U–MgO/P. However, almost same values of Caspase-3 activities were measured from the U–MgO/P and T-MgO/P groups (Fig. 4e), indicating that the difference was not result from apoptotic cell death.

To investigate the potential effects of the intracellular oxidative stress induced by the composite-created Mg^{2+} microenvironments as a mechanism of cellular damage, the reactive oxygen species (ROS) level of the cells cultured on U–MgO/P and T-MgO/P were measured (Fig. 4f). Compared with U–MgO/P group, the relative level of ROS decreased significantly by over 30% from the T-MgO/P group. The intracellular ATP level is also involved in the cell death. It is closely related to both *in vitro* and *in vivo* as a critical factor of the cell's decision to die through necrosis or apoptosis [33]. The ATP levels of the cells cultured on the U–MgO/T exhibited 16%- and 38%-reductions in comparison with the T-MgO/P group at day one and day three, respectively (Fig. 4g).

3.2.4. Investigation of in vitro macrophage behaviors on the biocomposites

The cell death rate and membrane integrity of the macrophages cultured on different biocomposites were also evaluated (Fig. 5a–c). Few cells died on the T-MgO/P, however, a dozen of dead cells appeared on the U–MgO/P, with the death rates at 3.66% and 13.78%, respectively. Significant differences of the LDH released in supernatant could be found between two groups. The leakage of the LDH from the T-MgO/P group was over 25% lower than from the U–MgO/P group.

Cellular morphologies exhibited on the U–MgO/P and the T-MgO/P biocomposites after a 3-day culturing were observed by SEM to evaluate the polarization of the macrophages (Fig. 5d). Small and elliptic cells with clear contour and lacking cytoplasmic extensions could be seen on the surface of T-MgO/P biocomposite, while high proportion of enlarged, dendritic stretched and fibriform cells, which were powerfully polarized macrophages [34], adhered on the U–MgO/P. With 2000 times magnification, distinct phenotype morphologies could be observed beside microscale holes (blue arrows) on the U–MgO/P (Figs. 5d–2). By using the flow cytometry method, high level of CD197-positive cells (28.2%) was detected on the U–MgO/P, while only 7.46% macrophages were polarized to pro-inflammatory phenotype from the T-MgO/P group (Fig. 5e). In contrast, ratios of the anti-inflammatory macrophage phenotype were low in both groups. Consistent with the SEM observation and the flow cytometry evaluation, cell cultured on the U–MgO/P biocomposite secreted significantly higher level of pro-inflammatory related genes IL6 (8-fold), CCR7 (3-fold), CD80 (9-fold) and TNF (2-fold) compared to the T-MgO/P group (Fig. 5f). All the anti-inflammatory related genes, however, showed no distinct differences between the two groups.

3.3. In vivo studies

3.3.1. Characterization of the 3D printed scaffolds

After a 3D-printing fabrication process, the surface morphologies along with the magnesium and carbon elements distribution of the scaffolds were observed (Fig. 6a). All the 3D scaffolds have been well established with structured geometry. Phase separation of the polymer matrix and MgO can be distinguished within the U–MgO/P, while only uniform material can be found in the T-MgO/P group. The element distribution of the U–MgO/P scaffold revealed that, MgO cluster with the size of dozen microns located inside the scaffold (figured out in the orange dashed circle). Homogeneous magnesium element distribution in correspondence with the carbon element distribution exhibited within the T-MgO/P scaffold.

3.3.2. Immune and foreign body responses within the subcutaneous implantation model

To comprehensively evaluate the foreign body responses induced by the different biocomposite-created Mg^{2+} microenvironments, the 3D-printed scaffolds were implanted subcutaneously into the animal model for 3, 7, 14 and 28 days. The H&E-stained photographs (Fig. 6b) showed that, numerous inflammatory cells were detected around the U–MgO/P scaffold, while fewer presented in T-MgO/P group at all time. The U–MgO/P scaffold displayed more inflammatory cell infiltration than the T-MgO/P within the implantation site. The following quantitative analysis confirmed that significant higher level of inflammatory cells could be found around the U–MgO/P than T-MgO/P scaffold (Fig. 6e). In parallel with the H&E staining, anti-CD68 immunofluorescence staining was performed to evaluate the macrophage-related inflammatory responses after implantation. The subcutaneous tissue surrounding the T-MgO/P scaffold had a gradually decreased immune

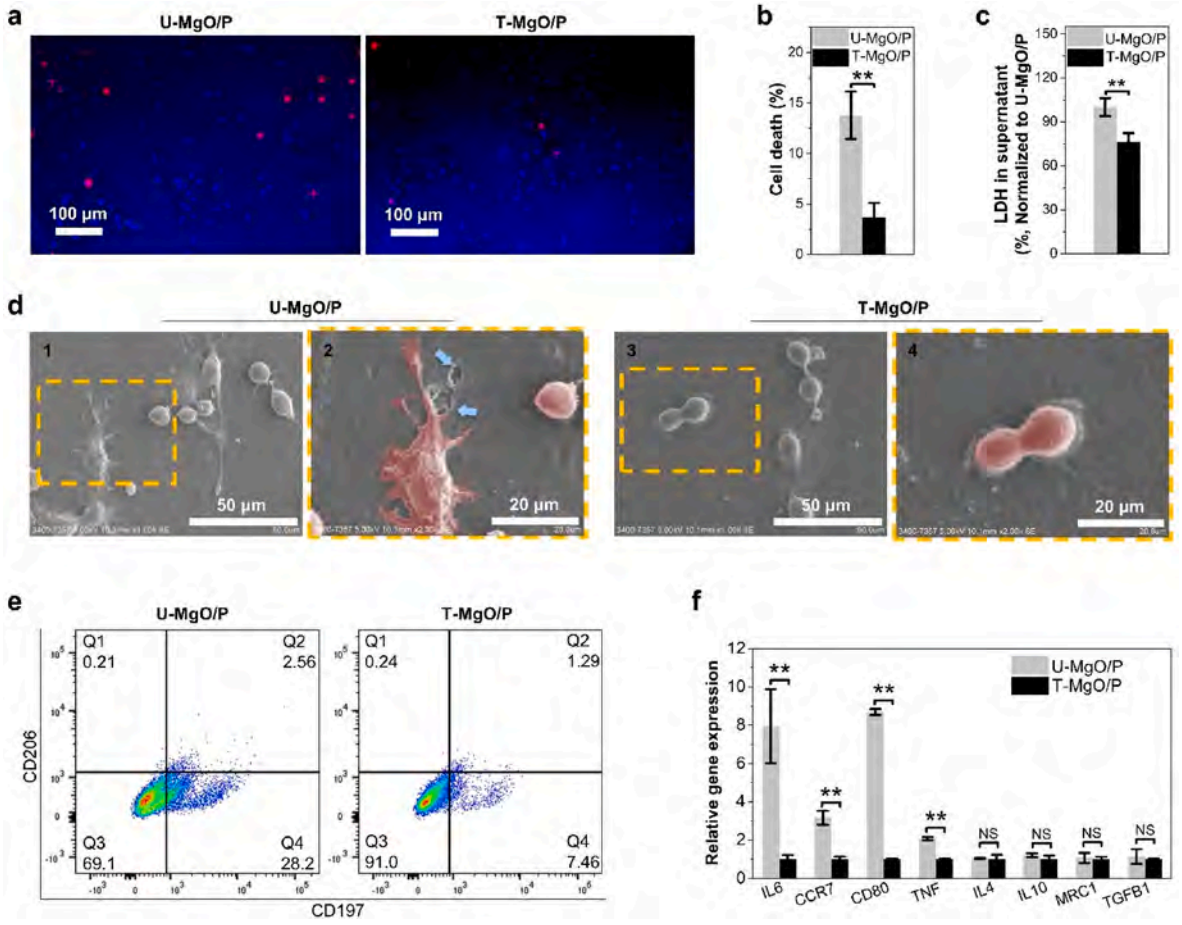

Fig. 5. Macrophage behaviors on U–MgO/P and T-MgO/P biocomposites. (a) Fluorescence microscopic observation and (b) quantitative analysis of the cell death rate of the RAW264.7 macrophages cultured for 3 days on the U–MgO/P and T-MgO/P. (c) The membrane integrity of cells cultured on U–MgO/P and T-MgO/P assessed by the LDH assay. The LDH leakage of the macrophages cultured on the T-MgO/P was also significantly lower than on the U–MgO/P. (d) 1000 times magnification SEM views of macrophages cultured on the 1) U–MgO/P and 3) T-MgO/P after 3 days to observe the cell morphologies and to evaluate the polarization of the macrophages. Scale bar: 50 μm. 2) U–MgO/P and 4) T-MgO/P with 2000 times magnification. Polarized macrophages would show distinct phenotype morphologies, e.g., enlargement, fibriform and dendritic stretch. Cells with dendritic morphology could be found around pores (blue arrows) on the U–MgO/P while cells remain rounded shape on the T-MgO/P. Scale bar: 20 μm. (e) Polarization of macrophages cultured on the U–MgO/P and T-MgO/P determined by flow cytometry. CD197 and CD206 were employed as the representative markers of the pro-inflammatory and anti-inflammatory macrophage phenotypes in this test. (f) Analysis of cell polarization via the mRNA expression level measurement. The mRNA expression levels of pro-inflammatory phenotype related markers and anti-inflammatory phenotype related markers were measured and normalized to the GAPDH. Cells cultured on the U–MgO/P expressed significantly higher levels of pro-inflammatory related genes compared to the T-MgO/P group while no distinct differences could be observed with anti-inflammatory related genes between the two groups. (**, $p < 0.01$; NS, no significant difference). (For interpretation of the references to color in this figure legend, the reader is referred to the Web version of this article.)

response from day 3 to day 14, while in the U–MgO/P group, the tissues displayed symptoms of severe immune responses over the course of the whole period (Fig. 6c). At each time point, the expression of CD68 in the T-MgO/P group was significantly lower than that of in the U–MgO/P group (Fig. 6f). Twenty-eight days post-operation, the U–MgO/P scaffold was encapsulated by thick and dense collagen layer, while the T-MgO/P group presented much less of the capsule (Fig. 6d and g).

3.3.3. *Immune responses within the bone defect model*

Histological and immunofluorescent analyses were also performed to evaluate the immune responses inside the bone defects induced by the different ionic niches. With a heterogeneous-composite created unbalanced Mg^{2+} microenvironment, considerable number of inflammatory cells presented at both time points (Fig. 7a and b). In contrast, significantly fewer immune cells could be found within a homogeneous-composite created ionic micro-homeostasis. Three-day and seven-day post-implantation, in the U–MgO/P group, high expressive level of pro-inflammatory macrophage related marker iNOS could be observed, meanwhile, the expression of anti-inflammatory related marker CD163 was absent. Moderate and mild expression of iNOS were shown in the T-MgO/P group at day 3 and day 7, respectively, while several macrophages polarized to anti-inflammatory phenotype and expressed CD163 after a 7-day implantation (Fig. 7c and d). Twenty-eight-day post-operation, the expression of the iNOS could be hardly detected, and high level of bone formation marker OCN was seen in the T-MgO/P group (Fig. 7e). On the contrary, implanted with the U–MgO/P scaffold, over 10 times higher iNOS and 15 times lower OCN expression were observed within the defect (Fig. 7f).

3.3.4. *Evaluation of new bone formation*

To evaluate the new bone formation within the defect sites, micro-CT and histological analysis were performed. Cross-section figures of the rat's femur with the view of the defect site (yellow dashed circle) and 3D reconstructed models of the implantation sites are exhibited in Fig. 8a. Even at 4 weeks post-operation, the U–MgO/P group had nearly no sign of new bone formation within the defect site. In contrast, moderate bone growth could be observed from the edge to the inward of the T-MgO/P scaffold after 4 weeks. Although almost the same values were seen

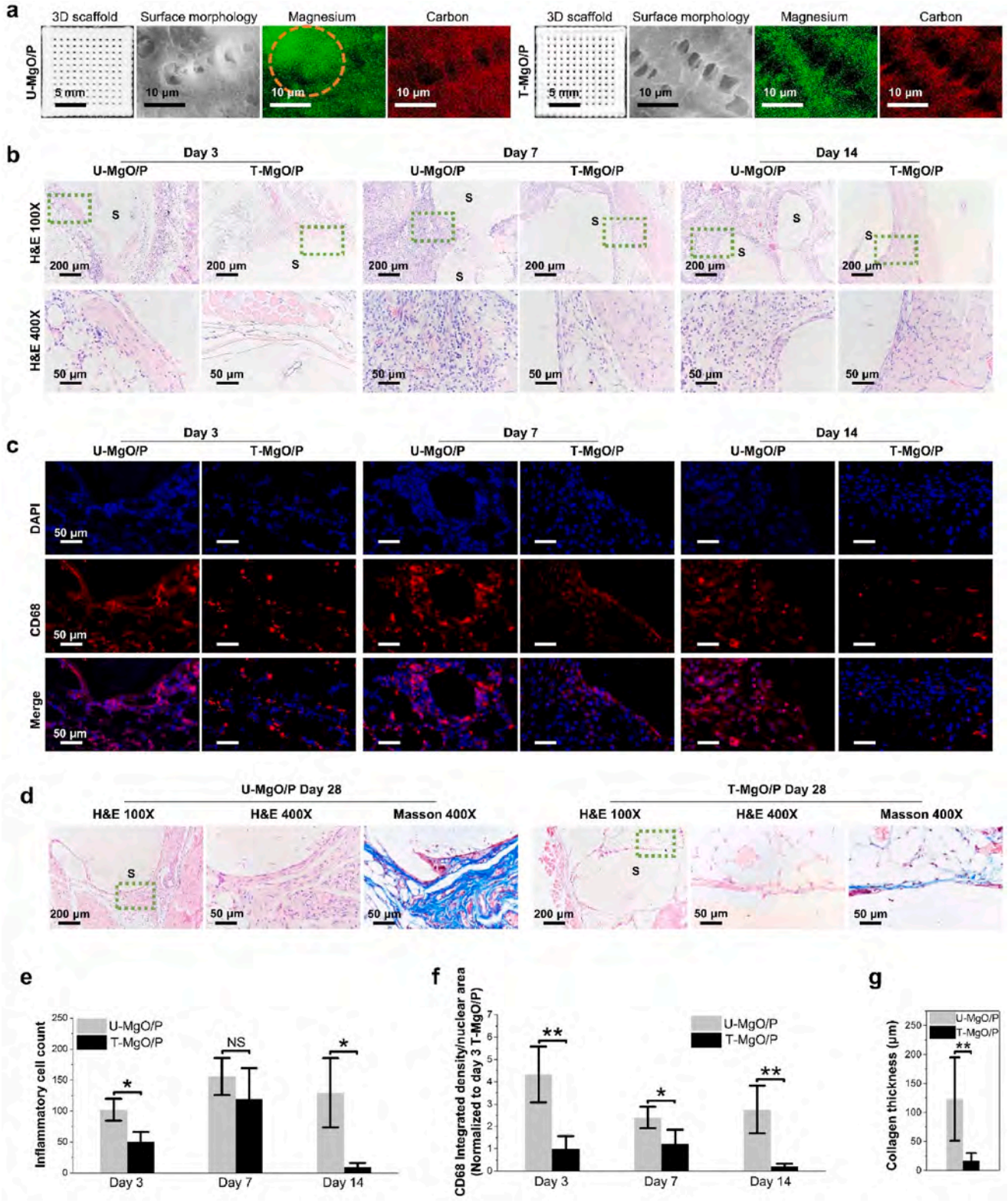

Fig. 6. Subcutaneous investigation of the post-operative immune responses caused by the scaffolds. (a) Morphological observation along with the corresponding magnesium and carbon element distributions of the 3D-printed scaffolds. The images show that the 3D-printed scaffolds in regular arrays have well-defined geometry. Heterogeneous distribution of magnesium oxide (figured out in the orange dashed circle) were successfully established within the U–MgO/P scaffold, while T-MgO/P scaffold exhibited evenly distributed magnesium element. Scale bar: 1st 5 mm; 2nd-4th 10 μm. (b) H&E stained histological photographs and (e) quantification of inflammatory cells in subcutaneous implanted model, where "S" denotes the location of the scaffolds, Scale bar: 1st row 200 μm; 2nd row 50 μm. (c) Immunohistofluorescence photographs and (f) quantification of the immunoresponses within the implantation sites, blue (DAPI), red (CD68). Scale bar: 50 μm. (d) Histological examination of collagen formation and (g) quantification of collagen thickness in tissues near subcutaneously implanted scaffolds 28-day post-operation. (*, $p < 0.05$; **, $p < 0.01$; NS, no significant difference). (For interpretation of the references to color in this figure legend, the reader is referred to the Web version of this article.)

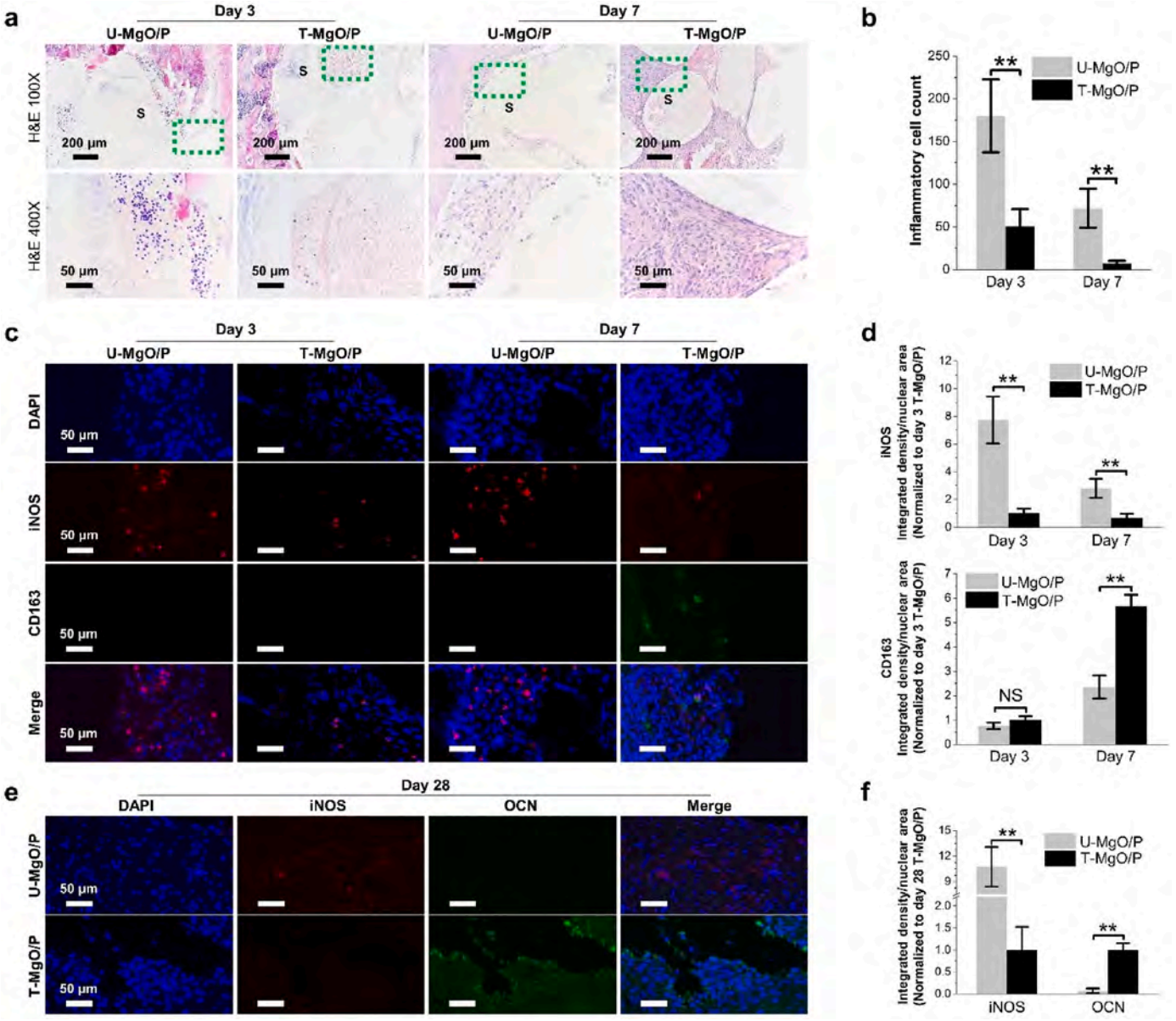

Fig. 7. Investigation of the post-operative immune responses caused by the scaffolds within bone defects. (a) H&E stained histological images and (b) quantification of inflammatory cells within the defect sites after implantation of the scaffolds for 3 and 7 days, where "S" denotes the location of the scaffolds, scale bar: 1st row 200 μm; 2nd row 50 μm. (c) Immunohistofluorescence photographs and (d) quantification of the immunoresponses within the implantation sites after 3- and 7-days implantation, blue (DAPI), red (iNOS) and green (CD163). Scale bar: 50 μm. (e) Immunohistofluorescence photographs and (f) quantification of the immunoresponses and bone formation within the implantation sites after 28-day implantation, blue (DAPI), red (iNOS) and green (OCN). Scale bar: 50 μm. (**, $p < 0.01$; NS, no significant difference). (For interpretation of the references to color in this figure legend, the reader is referred to the Web version of this article.)

between two groups after 2-weeks implantation, significantly higher increasing rate of the bone volume (4.5%) and bone mineral density (121.7%) could be found within the T-MgO/P scaffold 4-weeks post-operation (Fig. 8b and c). In the Giemsa-stained images (Fig. 8d), the dashed yellow curves indicate the interface of the defect areas in the femur, while mineralized bone is stained in purple color, the fibrous connective tissue and osteoblast are stained in blue. The U–MgO/P group exhibited that the defect region lacking of mineralized deposits. Four weeks post-surgery, only fibrous connective tissues with ordered spindle-shaped cells were present inside the defect area of the U–MgO/P scaffold. Although fibrous connective tissues can also be found within the T-MgO/P scaffold group, considerable amount of bone tissue newly formed from the edge of the defect. Affected by the heterogeneous-scaffold created unbalanced Mg^{2+} microenvironment, fibrous connective tissue without recognizable ossification point can be observed, whereas calcium deposition and new bone formation appeared within the homogenous-scaffold created Mg^{2+} micro-homeostasis (Supplementary Fig. 2). The mechanical performances of the newly formed bone were assessed by the nanoindentation test. The applied force act on the T-MgO/P group raised up dramatically with the displacement increase of the probe and finally met the maximum load at 99.8 N, whereas the U–MgO/P group showed a flattening growth of the loading curve, of which the highest load was only 23.0 N (Fig. 8e and f). Moreover, the modulus of the newly formed bone induced by the T-MgO/P was 5.1 GPa (Fig. 8g). In contrast, significantly lower value (1.6 GPa) was exhibited by the U–MgO/P group. Similar to the modulus results, surface hardness of the new bone induced by the U–MgO/P and T-MgO/P scaffolds were also significantly different from each other with the values of 24.6 MPa and 110.0 MPa, respectively (Fig. 8h).

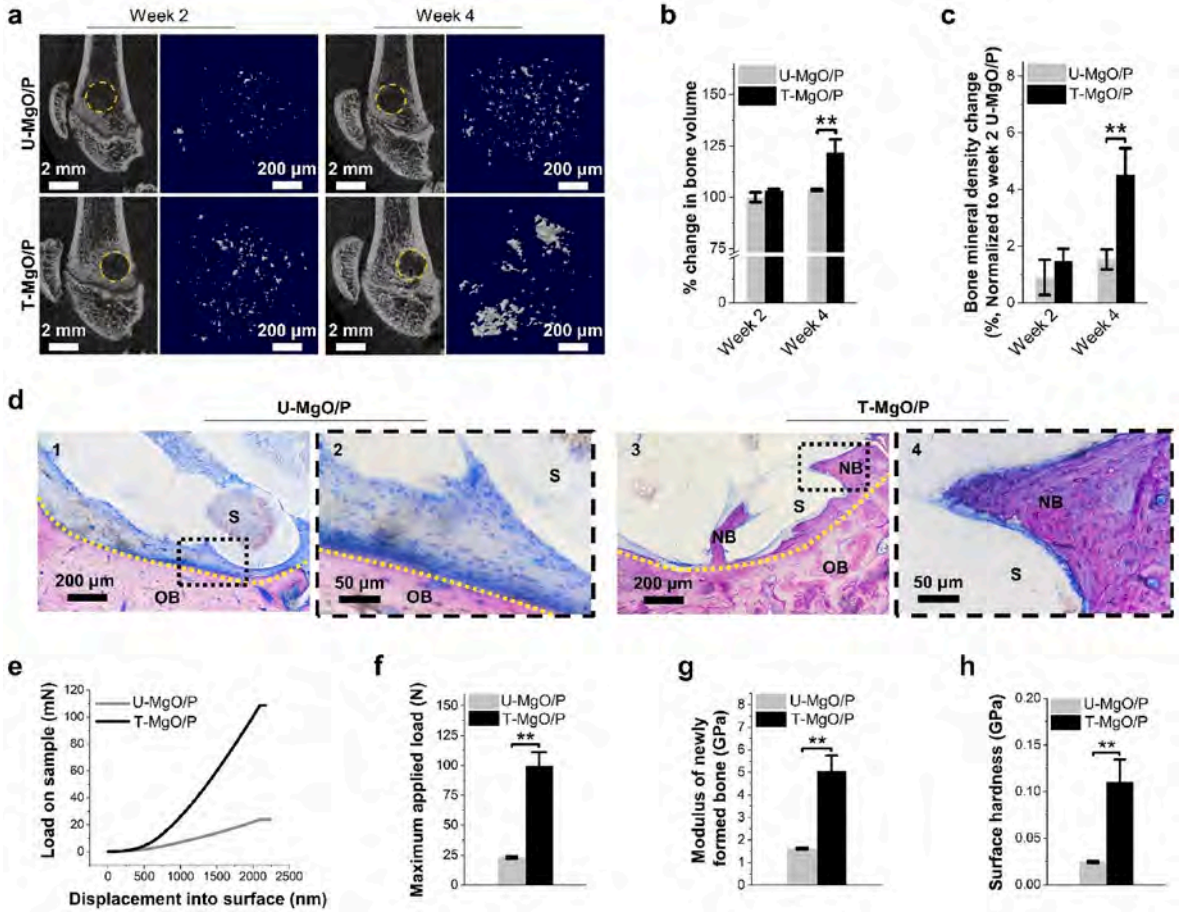

Fig. 8. ***In vivo*** **investigation of the bone tissue repairing within the scaffolds.** (a) Micro-CT images and 3D reconstruction models of the lateral epicondyle of the newly formed bone within the scaffolds (yellow dashed circles). Scale bar: 1st & 3rd columns 2 mm; 2nd & 4th columns 200 μm. Four weeks post-operation, new bone formed within the T-MgO/P scaffold while the U–MgO/P restricted the formation of bone. (b) The percentage changes of bone volume and (c) bone mineral density changes within the scaffolds 2-and 4-weeks post operation. Significantly higher increasing rate of the bone volume and bone mineral density could be found within the T-MgO/P scaffold as compared to the U–MgO/P group. (d) Histological photographs of the defect sites after implantation of the scaffolds for 4 weeks with Giemsa staining. 1) and 3) 100× magnification showing the bone/scaffold interfaces (yellow dashed curves) and new bone formation within the scaffolds. Scale bar: 200 μm. 2) and 4) 400× magnification showing the osteoblasts and fibrous connective tissues within the scaffolds. Scale bar: 50 μm 'NB', 'OB' and 'S' represented the location of newly formed bone, original bone and the scaffolds, respectively. (e)–(h) Mechanical properties of new formed bone within the scaffold 4-weeks post operation. (e) and (f) demonstrated the loading curves and maximum loading forces to the new bone from different groups, while (g) and (h) exhibited modulus and surface hardness of the newly formed bone tissues. (**, $p < 0.01$). (For interpretation of the references to color in this figure legend, the reader is referred to the Web version of this article.)

4. Discussion

Microenvironmental cues provided by the biomaterials are usually served as "mediators" in efforts to improve the biocompatibility and biodegradability of the materials, to regulate major cellular behaviors from cell adhesion to apoptosis or necrosis, to even guide the functional regeneration of tissues [35–38]. The modulation of those biological effects are sophisticated processes that require accurately regulated microenvironments, otherwise the biofunctionalization of the cues could be completely reversed [5,39–41]. In this study, we have demonstrated the significant impact of the bioactive factor magnesium ionic micro-homeostasis on cell fate modulation and the subsequent osteoimmunoregulation. Non-uniformity of biocomposite material can lead to the formation of voids and aggregations, which may create channels and defects for the ions to spread out to the external microenvironment [42]. After preparation of the biocomposites, the MgO nanoparticles are homogeneously or heterogeneously distributed in the polymeric matrix. With the infiltration of the water molecules, reaction between the MgO and water undergo evenly or unsteadily to form magnesium hydrate, and followed with generation of Mg^{2+}. Finally, the Mg^{2+} release of the homogeneous biocomposite is subjected to a diffusion-through-the-polymer-matrix mechanism [43], while the heterogeneous biocomposite release irregularly. Micron-sized MgO clusters along with inorganic/organic phase separation presented in the U–MgO/P, leading to an unbalanced microenvironment with erratic ion release, while the T-MgO/P have a visible even distribution of magnesium element, which provided a stable homogeneous ionic microenvironment.

Investigations in various cellular systems revealed that changes in cell spreading and morphologies are correlated with the tissue-specific gene expressions, growth of cells and conservation of differentiated functions [44–47]. On the T-MgO/P, the cells showed larger and extended morphologies with more projections around, indicating a better cell-substrate adhesion within a homogeneous-composite-created micro-homeostasis. Because the cellular morphologies can reflect the cytoskeletal alinements, which are partially regulated by the interactions between the surrounding environment and cells [45]. Moreover, cell adhesion and morphologies at the early-stage had a strong impact on cell proliferation, migration and differentiation [48,49]. The T-MgO/P which had better cell adhesion and morphologies showed on the surface therefore demonstrated better cellular proliferation property as compared to the U–MgO/P (Fig. 3). Interestingly, round and crimpled

as well as "escaping" cells are observed close to the microscale irregular holes on the U–MgO/P. To migrate towards or away from chemotactic cues, the development of asymmetrical projections around cellular periphery is a curtail step [50]. Hence, the phenomenon shown in the SEM image may due to the evasive movement to the high level of Mg^{2+} that caused by the burst release from those hole areas.

Cell death is the end point of cellular injury that induced by xenobiotics [51]. The results showed a significantly higher death rate of cells cultured within the heterogeneous-composite-created unbalanced ionic microenvironment. Generally, the death of cell has been distinguished into two modes, the accidental cell death and programmed cell death [52]. Caspase family is playing important role in programmed cell death apoptosis [53]. Among them, the activation of caspase-3 proteases was deemed as one of the crucial steps for the apoptosis [54]. Almost same values of Caspase-3 activities indicating that the difference was not result from apoptotic cell death. It was demonstrated that the death of cell on the U–MgO/P may went through the necrosis process, which is characterized by the losing of membrane integrity and swelling of the organelles and cytoplasm [52,55]. Possible mechanism of this necrosis may attribute to the raising of intracellular ROS level and depletion of the ATP content that induced by the perturbation of the Mg^{2+} microenvironment created by the micron-sized clusters (Fig. 9). Previously suggested hierarchical oxidative stress model, in which at a low level of oxidative stress can restore cell redox homeostasis while intermediate and high amount may induce pro-inflammatory responses and cell death, respectively [56]. Furthermore, the ATP is required in various effector processes during apoptosis whereas ATP-depleting condition shifts the cell toward a necrotic death [57].

Known as the host defense that protects against disease, the immune system is considered integral to tissue regeneration [58–60]. Macrophages, as the typical phagocytes of the immune system, are one of the most crucial cells associated with the biomaterial-triggered foreign body reactions [61]. Upon the heterogeneous-composite-created unbalanced release of the Mg^{2+}, a number of macrophage cells went through the necrotic process on the U–MgO/P. The death of macrophages by necrosis might result in the leakage of inflammatory cytokines and cellular proteases, which could initiate an augment inflammatory response [62–64]. Significantly higher proportion of macrophages were polarized towards the pro-inflammatory phenotype within this unbalanced microenvironment than that of the homogeneous-composite-created stable niche. Typically, the pro-inflammatory phenotypes generate high content of nitric oxides and pro-inflammatory cytokines that has double-edged consequences, promote host defense also damage healthy tissues, while anti-inflammatory macrophages decrease inflammation, mediate tissue repair and wound healing [65,66]. As a support, prolonged inflammatory stage and severe capsule formation were observed from the animal model encapsulated with heterogeneous U–MgO/P scaffold.

Growing number of evidences indicate that inflammatory signals are significant for the initiation of the bone healing process [67]. Magnesium insufficiency raises the level of pro-inflammatory cytokines, whereas magnesium could mediate the immunoregulation by increasing the content of nuclear factor of kappa light polypeptide gene enhancer in B-cells inhibitor, alpha (IκB-α) and decrease the generation of inflammatory cytokines, like IL-6 and TNF-α [68–70]. Additionally, in comparison with the extract of normal calcium phosphate cement, the extract of the magnesium-calcium phosphate cement turns down the inflammatory responses because of the interaction between the magnesium-containing milieu and macrophages [71]. However, the results of this study suggest that unexpected variables, such as the aggregation structure of bioactive factors, can have a great impact on the cellular behaviors and immune responses. The inflammatory and foreign body reactions within the bone defect can also be extended followed with delayed bone tissue regeneration when a heterogeneous-composite-created unbalanced Mg^{2+} ionic niche was provided (Fig. 10). Although, the spatiotemporal coordination of tens of thousands of molecules makes the cells adaptable to the environment, the drastic fluctuation of the microenvironment constructed by the biomaterial has the opportunity to cause serious damage to the cells. Indeed, cells are viable under a relatively narrow set of conditions. Breakdown of homeostatic regulation can lead to cell death or contribute to the cause or progression of diseases.

5. Conclusion

In conclusion, homogeneous- and heterogeneous-particle-embedded biocomposites were established using the biodegradable polymer PCL and MgO nanoparticles. Within a heterogeneous-composite-created unbalanced microenvironment, erratic ion niche was provided, while a homogeneous biocomposite creates a magnesium ionic micro-homeostasis over its entire surface. Compared with the micro-homeostasis, cells cultured in an unbalanced microenvironment not only showed impaired adhesion, that due to the restrained cell spreading and decreased membrane extensions, but also significantly down-regulated the expression of proliferation-related genes and caused cell cycle arrest. More seriously, raise of the intracellular oxidative stress and drop of the ATP content that induced by this unbalanced microenvironment leaded to a high ratio of necrotic cell death. The immunomodulation was also compromised by the perturbation of the Mg^{2+}. Higher proportion of macrophages polarized towards the pro-inflammatory

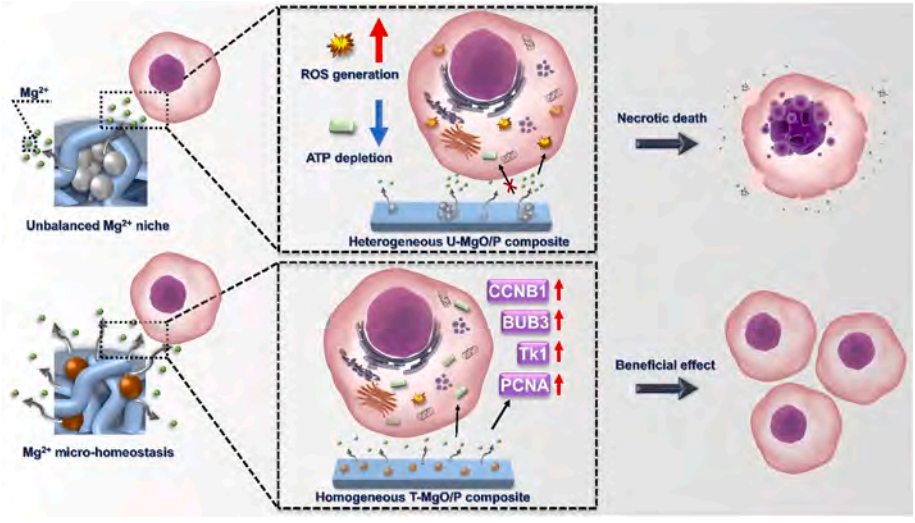

Fig. 9. Schematic illustration expounding the effect of biocomposite-mediated niches on cell fate regulation. Cells cultured in an unbalanced magnesium ionic micro-homeostasis would result in a high ratio of necrotic death caused by the raising of the intracellular oxidative stress and depletion of the ATP content, whereas a biocomposite-created stable magnesium ionic micro-homeostasis could lead to beneficial cellular behaviors, such as promoted cell adhesion and proliferation that arise from the increasing numbers of the membrane extensions and upregulated expression of proliferation genes.

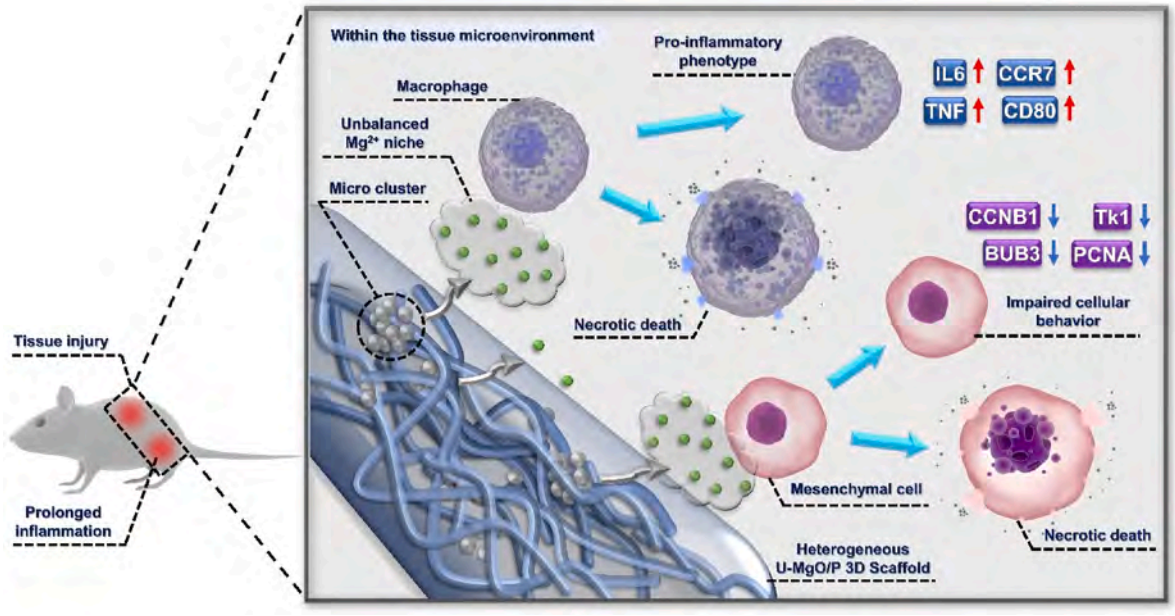

Fig. 10. Schematic illustration expounding the influence of biocomposite-mediated Mg^{2+} homeostatic perturbation on *in vivo* tissue regeneration. The unbalanced ionic niche established by the 3D scaffold may cause cell necrosis and motivate the nonactivated macrophage polarized towards pro-inflammatory phenotype, by which the immune responses and foreign body reactions were deteriorated and prolonged, leading to impaired and delayed tissue regeneration.

phenotype on the heterogeneous biocomposite. After the implantation of the heterogeneous U–MgO/P scaffold, serious and prolonged immune responses were induced, which leading to severe foreign body reactions and delayed bone tissue regeneration. Our results demonstrated that a perturbation of the Mg^{2+} niche that result from the heterogeneous micron-sized aggregation of MgO in the biocomposite could jeopardize the cellular behavior and tissue regeneration, which suggested that material-mediated micro-homeostasis of bioactive factors should be considered as a crucial part in designing and fabricating next generation of biomaterials.

Author statement

Jie Shen: Conceptualization, Validation, Formal analysis, Investigation, Writing-original draft, Writing-review and editing, Funding acquisition. Lei Yong: Validation, Formal analysis, Investigation, Writing-original draft. Bo Chen: Formal analysis, Resources. Wei Qiao: Methodology, Investigation. Xinyun Zhai: Methodology, Investigation, Resources. Shuhan Wang: Methodology. Yongcan Huang: Methodology, Formal analysis, Resources, Funding acquisition. Paul K. Chu: Methodology, Resources. Binsheng Yu: Formal analysis, Writing - review and editing, Funding acquisition. Kelvin W. K. Yeung: Conceptualization, Formal analysis, Writing-review and editing, Funding acquisition.

Declaration of competing interest

The authors declare that they have no known competing financial interests or personal relationships that could have appeared to influence the work reported in this paper.

Data availability

Data will be made available on request.

Acknowledgements

Jie Shen and Lei Yong contributed equally to this work. This work was financially supported by National Natural Science Foundation of China (82002303), Guangdong Basic and Applied Basic Research Foundation (Nos. 2022A1515011536, 2021A1515220093, and 2021A1515220086), Shenzhen Science and Technology Innovation Committee Projects (Nos. SGDX20220530111405038, JCYJ20190809182213535), the Peking University Shenzhen Hospital Scientific Research Funds (Nos. KYQD2021064, and KYQD2022215), Shenzhen Double Chain Project for Innovation and Development Industry supported by the Bureau of Industry and Information Technology of Shenzhen (No. 201806081018272960), Science and Technology Innovation Project of Foshan City (1920001000025), Health and Medical Research Funds (Nos. 09201466, 19180712), Hong Kong Research Grant Council General Research Fund (17214516).

Appendix A. Supplementary data

Supplementary data to this article can be found online at https://doi.org/10.1016/j.compositesb.2023.110961.

References

[1] Sadtler K, Estrellas K, Allen BW, Wolf MT, Fan H, Tam AJ, et al. Developing a pro-regenerative biomaterial scaffold microenvironment requires T helper 2 cells. Science 2016;352:366–70.
[2] Lutolf M, Hubbell J. Synthetic biomaterials as instructive extracellular microenvironments for morphogenesis in tissue engineering. Nat Biotechnol 2005; 23:47–55.
[3] Yu Y, Zhang W, Liu X, Wang H, Shen J, Xiao H, et al. Extracellular matrix scaffold-immune microenvironment modulates tissue regeneration. Compos B Eng 2022; 230:109524.
[4] Dong L, Yu W-M, Zheng H, Loh ML, Bunting ST, Pauly M, et al. Leukaemogenic effects of Ptpn11 activating mutations in the stem cell microenvironment. Nature 2016;539:304.
[5] Huang G, Li F, Zhao X, Ma Y, Li Y, Lin M, et al. Functional and biomimetic materials for engineering of the three-dimensional cell microenvironment. Chem Rev 2017;117:12764–850.
[6] Tu Z, Zhong Y, Hu H, Shao D, Haag R, Schirner M, et al. Design of therapeutic biomaterials to control inflammation. Nat Rev Mater 2022;7:557–74.
[7] Huang B, Tan L, Liu X, Li J, Wu S. A facile fabrication of novel stuff with antibacterial property and osteogenic promotion utilizing red phosphorus and near-infrared light. Bioact Mater 2019;4:17–21.
[8] Chen F-M, Liu X. Advancing biomaterials of human origin for tissue engineering. Prog Polym Sci 2016;53:86–168.
[9] Baptista D, Teixeira L, van Blitterswijk C, Giselbrecht S, Truckenmüller R. Overlooked? Underestimated? Effects of substrate curvature on cell behavior. Trends Biotechnol 2019;37:838–54.

[10] Zarrintaj P, Seidi F, Azarfam MY, Yazdi MK, Erfani A, Barani M, et al. Biopolymer-based composites for tissue engineering applications: a basis for future opportunities. Compos B Eng 2023;258:110701.
[11] Gomes BS, Simões B, Mendes PM. The increasing dynamic, functional complexity of bio-interface materials. Nat Rev Chem 2018;2:0120.
[12] Bei HP, Hung PM, Yeung HL, Wang S, Zhao X. Bone-a-Petite: engineering exosomes towards bone, osteochondral, and cartilage repair. Small 2021;17:2101741.
[13] Ramakrishna S, Mayer J, Wintermantel E, Leong KW. Biomedical applications of polymer-composite materials: a review. Compos Sci Technol 2001;61:1189–224.
[14] Maleki A, Ghomi M, Nikfarjam N, Akbari M, Sharifi E, Shahbazi M-A, et al. Biomedical applications of MXene-integrated composites: regenerative medicine, infection therapy, cancer treatment, and biosensing. Adv Funct Mater 2022;32:2203430.
[15] Chen C, Hou Z, Chen S, Guo J, Chen Z, Hu J, et al. Photothermally responsive smart elastomer composites based on aliphatic polycarbonate backbone for biomedical applications. Compos B Eng 2022;240:109985.
[16] Kim Y-M, He J, Biegalski MD, Ambaye H, Lauter V, Christen HM, et al. Probing oxygen vacancy concentration and homogeneity in solid-oxide fuel-cell cathode materials on the subunit-cell level. Nat Mater 2012;11:888–94.
[17] Tai K, Dao M, Suresh S, Palazoglu A, Ortiz C. Nanoscale heterogeneity promotes energy dissipation in bone. Nat Mater 2007;6:454–62.
[18] Noimark S, Colchester RJ, Blackburn BJ, Zhang EZ, Alles EJ, Ourselin S, et al. Carbon-nanotube–PDMS composite coatings on optical fibers for all-optical ultrasound imaging. Adv Funct Mater 2016;26:8390–6.
[19] Shadish JA, Benuska GM, DeForest CA. Bioactive site-specifically modified proteins for 4D patterning of gel biomaterials. Nat Mater 2019;18:1005–14.
[20] Rajagopal V, Bass G, Walker CG, Crossman DJ, Petzer A, Hickey A, et al. Examination of the effects of heterogeneous organization of RyR clusters, myofibrils and mitochondria on Ca2+ release patterns in cardiomyocytes. PLoS Comput Biol 2015;11:e1004417.
[21] Xu Y, Li J-J, Yu D-G, Williams GR, Yang J-H, Wang X. Influence of the drug distribution in electrospun gliadin fibers on drug-release behavior. Eur J Pharmaceut Sci 2017;106:422–30.
[22] Purushotham S, Ramanujan RV. Thermoresponsive magnetic composite nanomaterials for multimodal cancer therapy. Acta Biomater 2010;6:502–10.
[23] Freeman FE, Pitacco P, van Dommelen LH, Nulty J, Browe DC, Shin J-Y, et al. 3D bioprinting spatiotemporally defined patterns of growth factors to tightly control tissue regeneration. Sci Adv 2020;6:eabb5093.
[24] Shen J, Chen B, Zhai X, Qiao W, Wu S, Liu X, et al. Stepwise 3D-spatio-temporal magnesium cationic niche: nanocomposite scaffold mediated microenvironment for modulating intramembranous ossification. Bioact Mater 2021;6:503–19.
[25] Hutton DL, Moore EM, Gimble JM, Grayson WL. Platelet-derived growth factor and spatiotemporal cues induce development of vascularized bone tissue by adipose-derived stem cells. Tissue Eng 2013;19:2076–86.
[26] Qian Y, Lin H, Yan Z, Shi J, Fan C. Functional nanomaterials in peripheral nerve regeneration: scaffold design, chemical principles and microenvironmental remodeling. Mater Today 2021;51:165–87.
[27] Lu Y, Li H, Wang J, Yao M, Peng Y, Liu T, et al. Engineering bacteria-activated multifunctionalized hydrogel for promoting diabetic wound healing. Adv Funct Mater 2021;31:2105749.
[28] Shen J, Wang W, Zhai X, Chen B, Qiao W, Li W, et al. 3D-printed nanocomposite scaffolds with tunable magnesium ionic microenvironment induce in situ bone tissue regeneration. Appl Mater Today 2019;16:493–507.
[29] Wåhlander M, Nilsson F, Larsson E, Tsai W-C, Hillborg H, Carlmark A, et al. Polymer-grafted Al2O3-nanoparticles for controlled dispersion in poly(ethylene-co-butyl acrylate) nanocomposites. Polymer 2014;55:2125–38.
[30] Shabala SN, Newman IA, Morris J. Oscillations in H+ and Ca2+ ion fluxes around the elongation region of corn roots and effects of external pH. Plant Physiol 1997;113:111–8.
[31] Sgambato A, Wolf FI, Faraglia B, Cittadini A. Magnesium depletion causes growth inhibition, reduced expression of cyclin D1, and increased expression of P27KIP1 in normal but not in transformed mammary epithelial cells. J Cell Physiol 1999;180:245–54.
[32] Rubin H. The logic of the Membrane, Magnesium, Mitosis (MMM) model for the regulation of animal cell proliferation. Arch Biochem Biophys 2007;458:16–23.
[33] Tsujimoto Y. Apoptosis and necrosis: intracellular ATP level as a determinant for cell death modes. Cell Death Differ 1997;4:429.
[34] Wheeler KC, Jena MK, Pradhan BS, Nayak N, Das S, Hsu C-D, et al. VEGF may contribute to macrophage recruitment and M2 polarization in the decidua. PLoS One 2018;13:e0191040.
[35] Tabdanov ED, Puram VV, Win Z, Alamgir A, Alford PW, Provenzano PP. Bimodal sensing of guidance cues in mechanically distinct microenvironments. Nat Commun 2018;9:4891.
[36] Killaars AR, Grim JC, Walker CJ, Hushka EA, Brown TE, Anseth KS. Extended exposure to stiff microenvironments leads to persistent chromatin remodeling in human mesenchymal stem cells. Adv Sci 2019;6:1801483.
[37] Madl CM, Heilshorn SC. Engineering hydrogel microenvironments to recapitulate the stem cell niche. Annu Rev Biomed Eng 2018;20:21–47.
[38] Li M, Li L, Su K, Liu X, Zhang T, Liang Y, et al. Highly effective and noninvasive near-infrared eradication of a Staphylococcus aureus biofilm on implants by a photoresponsive coating within 20 min. Adv Sci 2019;6:1900599.
[39] Toh WS, Spector M, Lee EH, Cao T. Biomaterial-mediated delivery of microenvironmental cues for repair and regeneration of articular cartilage. Mol Pharm 2011;8:994–1001.
[40] Brafman DA. Constructing stem cell microenvironments using bioengineering approaches. Physiol Genom 2013;45:1123–35.
[41] Zhou Y, Wu C, Chang J. Bioceramics to regulate stem cells and their microenvironment for tissue regeneration. Mater Today 2019;24:41–56.
[42] Skrtic D, Antonucci JM, Eanes ED, Eidelman N. Dental composites based on hybrid and surface-modified amorphous calcium phosphates. Biomaterials 2004;25:1141–50.
[43] Chen B, Lin Z, Saiding Q, Huang Y, Sun Y, Zhai X, et al. Enhancement of critical-sized bone defect regeneration by magnesium oxide-reinforced 3D scaffold with improved osteogenic and angiogenic properties. J Mater Sci Technol 2023;135:186–98.
[44] Ben-Ze'ev A. The relationship between cytoplasmic organization, gene expression and morphogenesis. Trends Biochem Sci 1986;11:478–81.
[45] Ben-Ze'ev A, Robinson GS, Bucher NL, Farmer SR. Cell-cell and cell-matrix interactions differentially regulate the expression of hepatic and cytoskeletal genes in primary cultures of rat hepatocytes. Proc Natl Acad Sci USA 1988;85:2161–5.
[46] Yang R, Xue W, Ma X, Ren Y, Xu L, Kong W, et al. Engineering the dynamics of biophysical cues in supramolecular hydrogels to facile control stem cell chondrogenesis for cartilage regeneration. Compos B Eng 2023;250:110429.
[47] Fu J, Zhu W, Liu X, Liang C, Zheng Y, Li Z, et al. Self-activating anti-infection implant. Nat Commun 2021;12:6907.
[48] Ni P, Ding Q, Fan M, Liao J, Qian Z, Luo J, et al. Injectable thermosensitive PEG–PCL–PEG hydrogel/acellular bone matrix composite for bone regeneration in cranial defects. Biomaterials 2014;35:236–48.
[49] Hoque ME, San WY, Wei F, Li S, Huang M-H, Vert M, et al. Processing of polycaprolactone and polycaprolactone-based copolymers into 3D scaffolds, and their cellular responses. Tissue Eng 2009;15:3013–24.
[50] Shamloo A, Ma N, Poo M-m, Sohn LL, Heilshorn SC. Endothelial cell polarization and chemotaxis in a microfluidic device. Lab Chip 2008;8:1292–9.
[51] van Delft J, Mathijs K, Polman J, Coonen M, Szalowska E, Verheyen GR, et al. Chapter 5.1 - hepatotoxicity screening on in vitro models and the role of 'omics. In: Kleinjans J, editor. Toxicogenomics-based cellular models. San Diego: Academic Press; 2014. p. 193–212.
[52] Hotchkiss RS, Strasser A, McDunn JE, Swanson PE. Cell death. N Engl J Med 2009;361:1570–83.
[53] Fan T-J, Han L-H, Cong R-S, Liang J. Caspase family proteases and apoptosis. Acta Biochim Biophys Sin 2005;37:719–27.
[54] Brentnall M, Rodriguez-Menocal L, De Guevara RL, Cepero E, Boise LH. Caspase-9, caspase-3 and caspase-7 have distinct roles during intrinsic apoptosis. BMC Cell Biol 2013;14:32.
[55] Danial NN, Korsmeyer SJ. Cell death: critical control points. Cell 2004;116:205–19.
[56] Nel A, Xia T, Mädler L, Li N. Toxic potential of materials at the nanolevel. Science 2006;311:622–7.
[57] Eguchi Y, Shimizu S, Tsujimoto Y. Intracellular ATP levels determine cell death fate by apoptosis or necrosis. Cancer Res 1997;57:1835–40.
[58] Aurora AB, Olson EN. Immune modulation of stem cells and regeneration. Cell Stem Cell 2014;15:14–25.
[59] Min H, Li K, Wang Q, Gao X, Xie L, Tian W. A novel filler of biocomposites for long-term self-regulated delivery of immunomodulatory and antibacterial components to accelerate bone regeneration. Compos B Eng 2022;238:109942.
[60] Xie X, Mao C, Liu X, Tan L, Cui Z, Yang X, et al. Tuning the bandgap of photo-sensitive polydopamine/Ag3PO4/graphene oxide coating for rapid, noninvasive disinfection of implants. ACS Cent Sci 2018;4:724–38.
[61] Liu W, Li J, Cheng M, Wang Q, Yeung KW, Chu PK, et al. Zinc-modified sulfonated polyetheretherketone surface with immunomodulatory function for guiding cell fate and bone regeneration. Adv Sci 2018;5:1800749.
[62] Hanus J, Zhang H, Wang Z, Liu Q, Zhou Q, Wang S. Induction of necrotic cell death by oxidative stress in retinal pigment epithelial cells. Cell Death Dis 2013;4:e965–.
[63] Meng L, Jin W, Wang X. RIP3-mediated necrotic cell death accelerates systematic inflammation and mortality. Proc Natl Acad Sci USA 2015;112:11007–12.
[64] Tabas I. Consequences of cellular cholesterol accumulation: basic concepts and physiological implications. J Clin Invest 2002;110:905–11.
[65] Krausgruber T, Blazek K, Smallie T, Alzabin S, Lockstone H, Sahgal N, et al. IRF5 promotes inflammatory macrophage polarization and TH1-TH17 responses. Nat Immunol 2011;12:231–8.
[66] Lawrence T, Natoli G. Transcriptional regulation of macrophage polarization: enabling diversity with identity. Nat Rev Immunol 2011;11:750–61.
[67] Takayanagi H. Osteoimmunology: shared mechanisms and crosstalk between the immune and bone systems. Nat Rev Immunol 2007;7:292–304.
[68] Hu T, Xu H, Wang C, Qin H, An Z. Magnesium enhances the chondrogenic differentiation of mesenchymal stem cells by inhibiting activated macrophage-induced inflammation. Sci Rep 2018;8:3406.
[69] Weglicki WB, Phillips TM, Freedman AM, Cassidy MM, Dickens BF. Magnesium-deficiency elevates circulating levels of inflammatory cytokines and endothelin. Mol Cell Biochem 1992;110:169–73.
[70] Sugimoto J, Romani AM, Valentin-Torres AM, Luciano AA, Kitchen CMR, Funderburg N, et al. Magnesium decreases inflammatory cytokine production: a novel innate immunomodulatory mechanism. J Immunol 2012;188:6338–46.
[71] Wang M, Yu Y, Dai K, Ma Z, Liu Y, Wang J, et al. Improved osteogenesis and angiogenesis of magnesium-doped calcium phosphate cement via macrophage immunomodulation. Biomater Sci 2016;4:1574–83.

Supplementary Information

Effect of biocomposite mediated magnesium ionic micro-homeostasis on cell fate regulation and bone tissue regeneration

Jie Shen, Lei Yong, Bo Chen, Wei Qiao, Xinyun Zhai, Shuhan Wang, Yongcan Huang, Paul K. Chu, Binsheng Yu and Kelvin W. K. Yeung

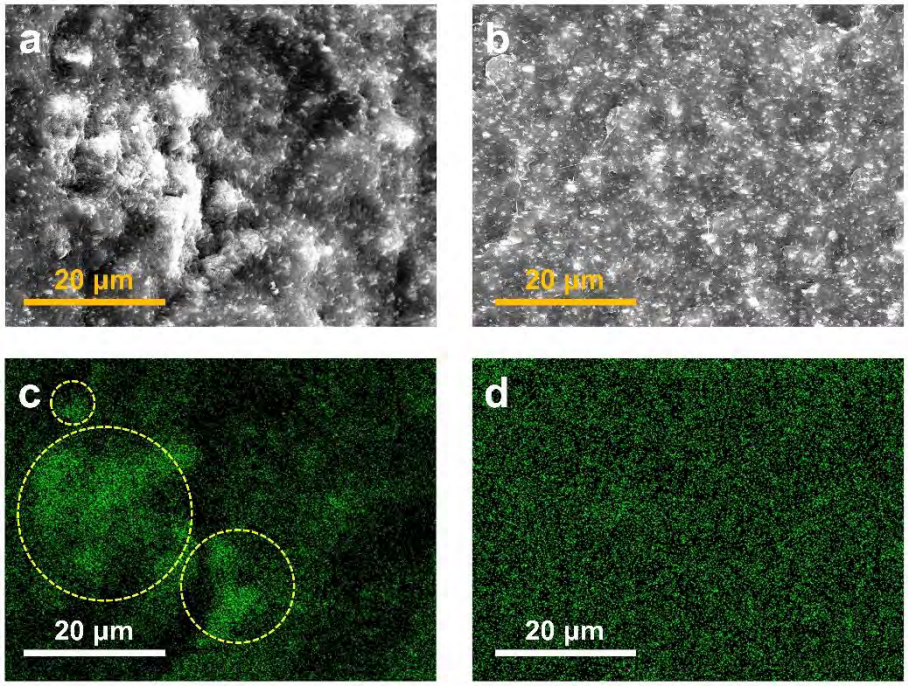

Supplementary Figure 1. Cross Section morphologies of the (a) U-MgO/P and (b) T-MgO/P; and the corresponding magnesium distribution of the (c) U-MgO/P and (d) T-MgO/P. Scale bar: 20 µm. Several micron-sized magnesium oxide clusters (yellow dashed circles) show from the area observed in U-MgO/P while the T-MgO/P have a visible homogeneous magnesium element distribution

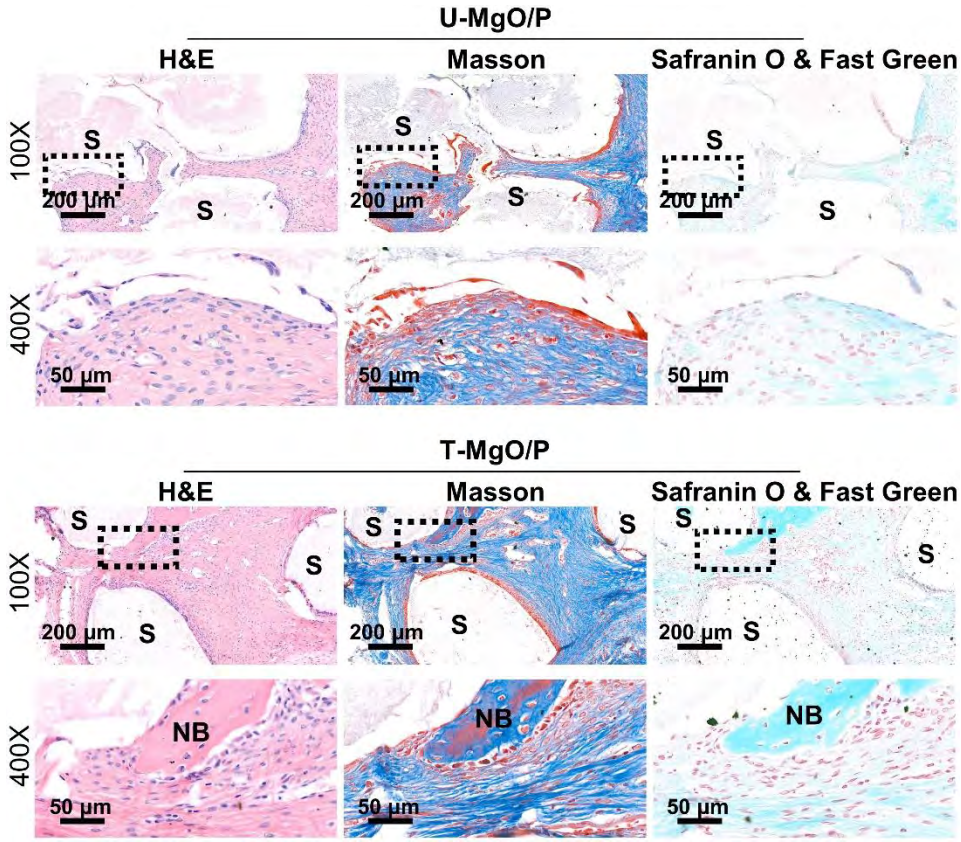

Supplementary Figure 2. H&E, Masson' s trichrome and Safranin O/Fast Green stained histological images of the defect sites after a 4-weeks implantation. Fibrous connective tissue without recognizable ossification point can be observed inside the defect implanted with U-MgO/P scaffold, whereas calcium deposition and new bone formation appeared within the T-MgO/P scaffold implanted defect. 'NB' and 'S' represented the location of newly formed bone and the scaffolds, respectively.

Supplementary Table 1 *Primer pairs used in real-time PCR analysis*

Gene	Forward primer	Reverse primer
GAPDH	5'-ACCCAGAAGACTGTGGATGG-3'	5'-CACATTGGGGGTAGGAACAC-3'
CCNB1	5'-AAGGTGCCTGTGTGTGAACC-3'	5'-GTCAGCCCCATCATCTGCG-3'
TK1	5'-AGTGCCTGGTCATCAAGTATGC-3'	5'-GCTGCCACAATTACTGTCTTGC-3'
BUB3	5'-GATGGCATCTCCTCGGTTAAG-3'	5'-AATTGGCGGGCACATCGTAG-3'
PCNA	5'-TTTGAGGCACGCCTGATCC-3'	5'-GGAGACGTGAGACGAGTCCAT-3'
IL6	5'-TAGTCCTTCCTACCCCAATTTCC-3'	5'- TTGGTCCTTAGCCACTCCTTC-3'
CCR7	5'- TGTACGAGTCGGTGTGCTTC-3'	5'- GGTAGGTATCCGTCATGGTCTTG-3'
CD80	5'- ACCCCCAACATAACTGAGTCT-3'	5'- TTCCAACCAAGAGAAGCGAGG-3'
TNF	5'- CCCTCACACTCAGATCATCTTCT-3'	5'- GCTACGACGTGGGCTACAG-3'
IL4	5'- GGTCTCAACCCCCAGCTAGT-3'	5'- GCCGATGATCTCTCTCAAGTGAT-3'
IL10	5'- GCTCTTACTGACTGGCATGAG-3'	5'- CGCAGCTCTAGGAGCATGTG-3'
MRC1	5'- CTCTGTTCAGCTATTGGACGC-3'	5'- CGGAATTTCTGGGATTCAGCTTC-3'
TGFB1	5'- CTCCCGTGGCTTCTAGTGC-3'	5'- GCCTTAGTTTGGACAGGATCTG-3'